https://doi.org/10.5194/egusphere-2023-3146
Preprint. Discussion started: 5 January 2024

Development of deformational regimes and microstructures in the deep sections and overall layered structures of the Dome Fuji ice core, Antarctica

Tomotaka Saruya[1], Atsushi Miyamoto[2], Shuji Fujita[1,3], Kumiko Goto-Azuma[1,3], Motohiro Hirabayashi[1], Akira Hori[4], Makoto Igarashi[1], Yoshinori Iizuka[5], Takao Kameda[4], Hiroshi Ohno[4], Wataru Shigeyama[3*], Shun Tsutaki[1,3]

[1] National Institute of Polar Research, Tokyo 190-8518, Japan
[2] Institute for the Advancement of Graduate Education, Hokkaido University, Sapporo 060-0817, Japan
[3] Polar Science Program, Graduate Institute for Advanced Studies, SOKENDAI, Tokyo 190-8518, Japan
[4] Kitami Institute of Technology, Kitami 090-8507, Japan
[5] Institute of Low Temperature Science, Hokkaido University, Sapporo 060-0819, Japan

[*]Currently at: JEOL Ltd., Tokyo, Japan

Correspondence: Tomotaka Saruya (saruya.tomotaka@nipr.ac.jp)

An in-depth examination of rheology within the deep sections of polar ice sheets is essential for enhancing our understanding of glacial flow. In this study, we investigate the crystalline textural properties of the 3035-m-long Antarctic deep ice core, with a particular emphasis on its lowermost 20%. We examine the crystal orientation fabric (COF) and compare it with various other properties from the ice core. In the uppermost approximately 80% thickness zone (UP80%), the clustering strength of single pole COF steadily increased, reaching its possible maximum at the bottom of the UP80%. Below 1800 m in the UP80%, layers with more or fewer dusty impurities exhibit slower or faster growth of cluster strength. This situation continued until 2650 m. In the remaining lowermost approximately 20% thickness zone (LO20%), the trend of the COF clustering strength changed around 2650 m and exhibited substantial fluctuations below this depth. In more impurity-rich layers, stronger clustering is maintained. In impurity-poor layers, relaxation of the COF clustering occurred due to the emergence of new crystal grains with *c*-axis orientation distinctly offset from the existing cluster, and dynamic recrystallization related to this emergence. The less impure layers show apparent features of bulging and migrating grain boundaries. We argue that the substantial deformational regime of polar ice sheets involves dislocation creep in both UP80% and LO20%, with dynamic recrystallization playing a critical role in the LO20%, particularly in impurity-poor layers, to recover a potential of COF available for the continuation of dislocation-creep-based deformation. Furthermore, we observe that layers and cluster axes of COF rotate meridionally due to rigid-body rotation caused by simple shear strain above subglacial slopes. These features provide vital clues for the development of the 3D structure of polar ice sheets in the deeper part, leading to inhomogeneous deformation between layers in various thickness scales, and the formation of folds, faults and mixing depending on the layers.

https://doi.org/10.5194/egusphere-2023-3146
Preprint. Discussion started: 5 January 2024

1. Introduction

The polar ice sheets are massive bodies of ice on Earth. With ongoing global warming, there is a deep concern about the trend of these ice sheets contributing to sea level rise (e.g., Church et al., 2013). Continuous improvement of reliable predictive models for this phenomenon is crucial. However, there are many key processes that govern the flow of ice sheets, making the modelling of these sheets complex. Although many essential processes exist, many are not included in modelling efforts due to insufficient understanding (e.g., Pattyn et al., 2008). Deciphering the dynamic layer structure within the ice sheet is one of the most critical challenges (e.g., Young et al., 2017). For instance, during the internal deformation of the ice sheet, the flow is modulated based on the crystal orientation fabric (COF), the concentration of ionic species and microparticles, as well as disturbances or folds in the layer structure (e.g., Cuffey and Paterson, 2010, Saruya et al., 2022b). These factors can introduce either positive or negative feedback, modulating the flow characteristics of the ice sheet. We need a systematic understanding of the layered internal structure of polar ice sheets over space and time. An important method for understanding these is to conduct dynamical analysis on ice cores, which provides a “ground truth” perspective of the ice. Furthermore, retrieving continuous ice core records that correspond to ages of more than 1 million years presents a significant challenge in palaeoclimatology (e.g., Wolff et al., 2022). International Partnerships in Ice Core Sciences (IPICS) identified the retrieval of multiple ice cores that extends to 1.5 million years (symbolically named as the oldest-ice cores) as one of the most important challenges for ice core studies. Identifying suitable sites for drilling of such ice will require knowledge of englacial layers under various ice conditions.

In ice sheets, the rheology in deep ice is complicated by geothermal effects and increased stresses from bedrock topography. So far, there have been limited reports on the crystal properties of ice near the bed in ice sheets (e.g., Durand et al., 2009, Faria et al., 2014a, Ohno et al., 2016). The Dome Fuji (DF) ice core was drilled on the Antarctic plateau, as shown in Figure 1. This location is at 77°19' S latitude and 39°42' E longitude, and 3,810 m above sea level. Annual surface mass balance (SMB) has ranged from approximately 24 to 28 kg m^{-2} y^{-1} over the last 5000 years (Oyabu et al., 2023), and the annual mean surface air temperature is –54.4°C (Yamanouchi et al., 2003). For the DF ice core, Ohno et al. (2016) revealed the air hydrates and water isotope composition of the deepest 1% thickness (3000–3035 m). These properties were found to retain the basic layered structure of ice core signals except in the deepest few meters. However, the investigation did not include the crystal orientation fabric (COF). For the EPICA Dome C (hereinafter referred to as EDC) Antarctic deep core (Figure 1), Durand et al. (2009) investigated the COF of ice down to the very deep parts, using thin sections of ice (40 × 110 mm in width and 0.4 mm in thickness) sampled at every 11 m depth.

The COF is one of important features for understanding ice dynamics. It contains information of deformational history, grain growth and recrystallization (e.g., Cuffey and Paterson, 2010; Faria et al., 2014a, b). Saruya et al. (2022b) investigated the layer structures of COF in the uppermost (shallower) ca. 80% thickness zone (hereinafter, UP80%) of the DF ice core. They used thick sections of ice (ranging in thickness from 33 to 79 mm) employing the principle of the radio-wave birefringence to obtain information from a volume much larger than that of thin sections of ice. The sampling volumes between the two methods (thick-section method and thin-section method) differ by a factor of 85–190. Using the dielectric tensor method (hereinafter, DTM), they continuously measured "dielectric anisotropy" (denoted as $\Delta\varepsilon$) along the ice cores with high resolution, involving ice volumes of cylinders measuring 16–38 mm in effective radio beam diameter and 33–79 mm in radio propagation thickness. This $\Delta\varepsilon$ is defined as the difference in relative permittivity along the vertical (denoted as ε_v) and in the horizontal plane (denoted as ε_h). Thus, $\Delta\varepsilon = \varepsilon_v - \varepsilon_h$. $\Delta\varepsilon$ is an indicator of the clustering strength of COF. $\Delta\varepsilon$ is linearly compatible with the normalized eigenvalues of the second order tensor (Saruya et al., 2022a, b). The normalized eigenvalues are often used to express degree of the COF clustering. Thus, continuous profiling with DTM is an innovative and powerful tool. These authors found that $\Delta\varepsilon$ steadily increases with depth, showing fluctuations in the UP80%. In addition, significant decreases in $\Delta\varepsilon$ were found at depths of major glacial to interglacial transitions. These changes in $\Delta\varepsilon$ are explained as variations in the deformational history. Moreover, fluctuations in $\Delta\varepsilon$ along neighbouring depths were enhanced during the glacial/interglacial transitions. Furthermore, the $\Delta\varepsilon$ data exhibited a positive correlation with the concentration of Cl^- ions and an inverse correlation with the amount of dust particles. Since these factors originate from atmospheric deposition, Saruya et al. (2022b) proposed that the fluctuations in COF might be common across wide area of ice sheets.

Following this previous study, research focusing on the lowermost (deepest) approximately 20% thickness zone (ranging from about 2400 m to the deepest ice at 3035 m) remains. Hereinafter, we refer to this zone as LO20%. A major difficulty was the inclination of the ice sheet layers, which became steeper at deeper depths (Dome Fuji Ice Core Project Members hereinafter referred to as DFICPM, 2017). In the present study, we extend the investigation to the LO20%. To investigate this, we utilized the thick-section-based method of (i) DTM, and thin-section-based methods such as (ii) the Laue X-ray diffraction method and (iii) the automatic ice fabric analyzer. We compare these textural data with various data from ice core analyses. This paper provides a comprehensive dataset of COF and other textural data. We then discuss COF development, variations in the microstructure, layered structures, and rheology of polar ice sheets. Our new data will provide important clues for understanding the development of the layer structure of ice sheets, which leads to inhomogeneous deformation of layers across various layer thickness scales. Note that a list of abbreviation is provided in Appendix A for clarity of terms used in this paper.

2. DF ice cores

At Dome Fuji (DF), deep ice cores have been drilled twice (e.g., Motoyama et al., 2020). The first core, "DF1" measuring 2503 m in length, was drilled in the 1990s. The second, "DF2," a 3035-m-long core, was drilled between 2004 and 2007 in a borehole 44 m away from (Figure 1c). We used the DF2 core in this study. The drilling sites are situated above a subglacial slope, positioned between bedrock high in the east and a subglacial trough with an ice thickness of about 3100 m in the west (Figures 1b and 1c). An ice thickness of about 2850 m marks the boundary between thawed bed (in thicker ice) and a frozen bed (in thinner ice) (Fujita et al., 2012). It is speculated that spatially inhomogeneous basal melting has caused the layer inclination in localized areas within the ice sheet (DFICPM, 2017). The layered structures incline by less than about 5° in the UP80% while in the lower 20% (LO20%), the inclination reaches values up to 45° at a depth of 3000 m.

https://doi.org/10.5194/egusphere-2023-3146
Preprint. Discussion started: 5 January 2024

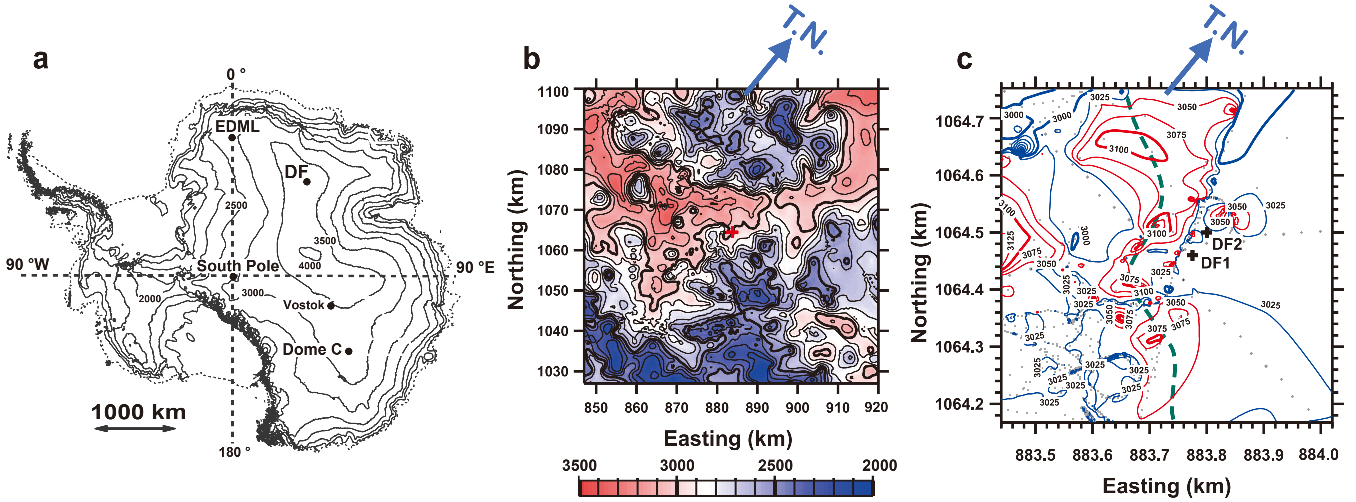

Figure 1. Maps of the Coring Site. (a) Surface elevation (DEM by Bamber et al., 2009). (b) and (c) show the thickness of the ice in areas of 72 km square, and 580 m square, respectively. Marker symbols near the center indicate the coring site. T.N. stands for true north. In (c), data points for ice thickness are represented by dots for the data from Tsutaki et al. (2022) and by markers for the data from Eisen et al. (2020). A green bold dashed line indicates the presence of the local trough. The DF coring sites are located at the bank of this local trough, aligning with the estimated drainage routes of subglacial water (as shown in Figure 8d in Tsutaki et al., 2022).

3. Methods and samples

3.1 Dielectric Tensor Method

3.1.1 Method

The principle of the open resonator method for determining the relative permittivity (ε) of thin samples have been described in the literature (Jones, 1976a, b; Cullen, 1983; Komiyama et al., 1991). We have developed this into a method for measuring the tensorial permittivity of thick samples by using radio birefringence continuously along ice cores (Matsuoka et al., 1998, Fujita et al., 2009, 2016, Saruya et al., 2022a, b, Inoue et al., 2023). We apply a microwave beam to thick samples. The ε values are volume-weighted averages within the volume encompassed by the Gaussian distribution of the beam. By setting the angle between the axis of the *c*-axes cluster and the electric field to approximately 45°, radio birefringence occurs due to macroscopic permittivity of the crystals (e.g., Hargreaves 1978). When we sweep radio frequencies to detect resonances satisfying TEM $_{0,0,q}$ modes (where TEM stands for transverse electromagnetic and q is an integer), we detect twin resonant peaks caused by the two permittivity components. These two components correspond to ε along the axis of the *c*-axes cluster and its orthogonal axis, representing components on the plane of the electric field vector (orthogonal to the axis of beam incidence).

3.1.2 The open resonators and samples

We utilized an open resonator (No.1 in Table 1) for the ice in the LO20%. This resonator is different from the resonator used for the ice in the UP80% (No.2 in Table 1). The two resonators, each having a semi-confocal shape with a flat mirror and a concave mirror, are designed to produce beam diameter of 16 mm and 38 mm, respectively. The consistency of the data obtained with the two resonators was confirmed by comparing the $\Delta\varepsilon$ values at depths between 2400 and 2500 m (Appendix B). The standard deviations (SD) from the No.1 resonator are slightly larger than those from the No.2 because of the smaller size of the beam (thus smaller volume of ice). The smaller beam size means that the No.1 resonator is available for smaller sized samples (for example, narrow quadrangular prism samples) and for higher spatial resolution measurements. The No.1 and the No.2 resonators can measure ice thickness at least 40 mm and 90 mm, respectively. This implies that with the small beam size, we can measure a large volume of ice in a single measurement. Sizes of the samples are given in Table 2. Both upper and lower surfaces were microtomed to make very smooth and precisely parallel surfaces. The age of the ice in the LO20% ranged from approximately 300 and 720 thousand years. The sampling rate for the DTM involves continuous 20 mm step measurements along a 0.5-m-long core segment from every 2.5-m depth interval. For samples deeper than 2736 m, we rotated the core axis horizontally in the open resonator setup to achieve detectable twin resonances. The experimental temperatures were in a range of –30 ± 1.5 °C.

Along with the increased layer inclination, the axis of the *c*-axes cluster also exhibited an increased inclination, deviating from the vertical. We refer to the meridional Inclination Angle of the *c*-axes Cluster from the vertical as the IACC. Additionally, the horizontal orientation of the *c*-axes cluster varied with depths due to the rotation of the ice cores. We designate the Horizontal Orientation of the *c*-axes Cluster as HOCC. Under conditions where both IACC and HOCC change with depths, we measure only the non-principal components of the permittivity tensor within the ice using DTM. To apply geometrical corrections from the measured non-principal components to the principal components, we utilized information of both IACC and HOCC, derived from COF data measured using thin-section methods. The procedures for these corrections are detailed in Appendices C and D. The non-principal components of the dielectric anisotropy ($\Delta\varepsilon'$) were adjusted to align with the principal components ($\Delta\varepsilon$).

Table 1: Specifications of the two resonators

Item	Curvature radius of the concave mirror (mm)	Distance between two mirrors (mm)	Scale diameter of the beam on the flat mirror (mm)	Frequencies (GHz)	Depths range (m)
Symbol	R	D	ω	f	z
Resonator No.1	120	110	16	26.5– 40	2400–2970
Resonator No.2	250	225	38	14–20	100–2500

Table 2: Thickness and width of the samples

Depths range (m)	Thickness (mm)	Width (mm)	Resonators used
2400–2500	35–37	53–58	No.1 and No.2
2500–2970	41–42	30–38	No.1

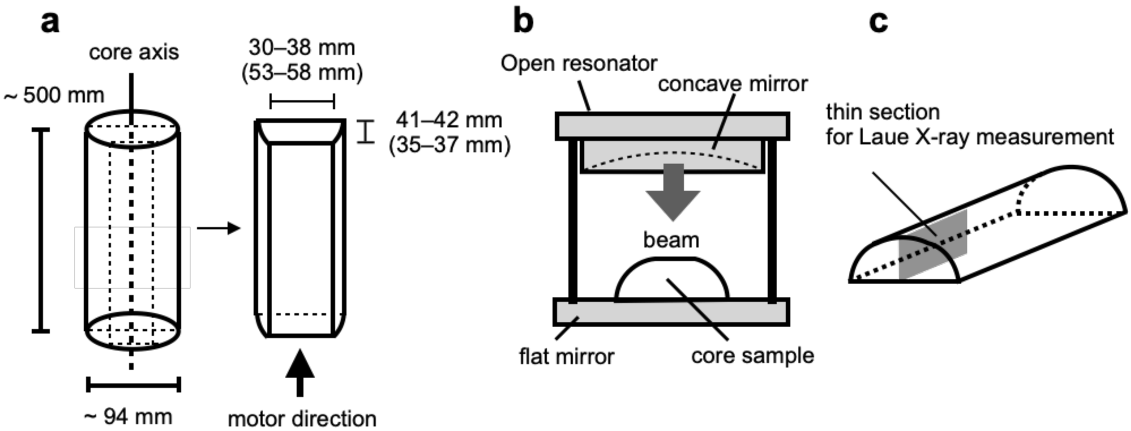

Figure 2. Diagrams of the (a) core cutting geometry, (b) setup viewed from the front, and (c) location of a thin section for the Laue X-ray diffraction measurements.

3.2 Laue X-ray diffraction method, the automatic fabric analyzer method and microstructure observations

The Laue X-ray diffraction method was applied to thin sections measuring 100 mm × 100 mm and with a thickness of less than 0.5 mm. This method can determine the orientations of all axes of each crystal grain with high accuracy and a spatial resolution of approximately less than 0.5 mm (Miyamoto et al., 2011). 43 depths within the thickness of the LO20% were selected. After obtaining all the Laue figures, the Laue patterns were analyzed. In each thin section, we express the data as the distribution of *c*-axes and *a*-axes on the Schmidt net diagram. Subsequently, the IACC and the HOCC—both are essential for the correction from $\Delta\varepsilon'$ to $\Delta\varepsilon$ (see Appendices C and D) —were calculated. In addition, we calculated the Median Inclination of *c*-axes with reference to the axis of the *c*-axes Cluster (hereinafter MICC). The MICC is defined as a half apex angle of the cone in which a half of the measured *c*-axes are included from the center axis of the *c*-axes cluster.

COF data were added using an automatic fabric analyzer model G50 manufactured by Russel–Head Instruments. Additionally, we conducted microstructure observations using optical microscopy on the same thin sections. These measurements were performed at several selected depths. We prepared thin sections from the vertical plane of the ice cores, measuring 90 mm in the depth direction, 50 mm in the horizontal direction, and 0.5 mm in thickness.

3.3 Grain size and layer inclination measurements

https://doi.org/10.5194/egusphere-2023-3146
Preprint. Discussion started: 5 January 2024

Grain sizes were measured at the DF site. Operators from the ice processing team observed the crystal grains by noting a faint difference in light reflectivity between grains and visible grain boundaries (hereinafter GB). While freshly cut surfaces did not exhibit such features, the ice cores in storage developed them over time due to the progress of sublimation. To measure the average surface area of each grain, we used three circular gauges with diameters of 10, 20, and 40 mm. The number of grains on the core surface within the circle of the gauge was counted. The number of crystal grains within each circle typically ranged from several to 20. The estimated error was up to 20%. This measurement was performed every 1.5 m to a depth of 2967.5 m. Below this depth, because of very large crystals, it was difficult to define grain size. Additionally, we visually investigated the growth of the Inclination Angle of the Visible Layers (IAVL), such as cloudy bands or tephra layers, from the horizon using a protractor. In this process, core rotation resulting from core breaks was not considered. In addition to our preliminary report on this point (DFICPM, 2017), this study provides detailed data.

4. Results

4.1 Depth-dependent variation in $\Delta\varepsilon'$

Results on $\Delta\varepsilon'$ are presented in Figure 3. Dots represent raw data. Examples of the continuous variation of $\Delta\varepsilon'$ along 0.5-m core segment are provided in Appendix E. Markers and bars indicate the average values and the standard deviations (SD) determined at 0.5-m intervals along the core sample. Black and red symbols represent data obtained without and with inclined measurement, respectively. Data from both cases (without and with horizontal sample inclinations within the resonator) in agreement at overlapping depths (2630–2730 m), confirming the experimental principle that the horizontal rotation of the samples in the open resonator give no influence on the measurement of the relative permittivity. We note that in the LO20% $\Delta\varepsilon'$ values have a large-scale tendency to decrease with increasing depth. The scatter of the raw data tends to be larger at greater depths. We will discuss the detailed features after applying necessary corrections, using results from the Laue X-ray diffraction measurements.

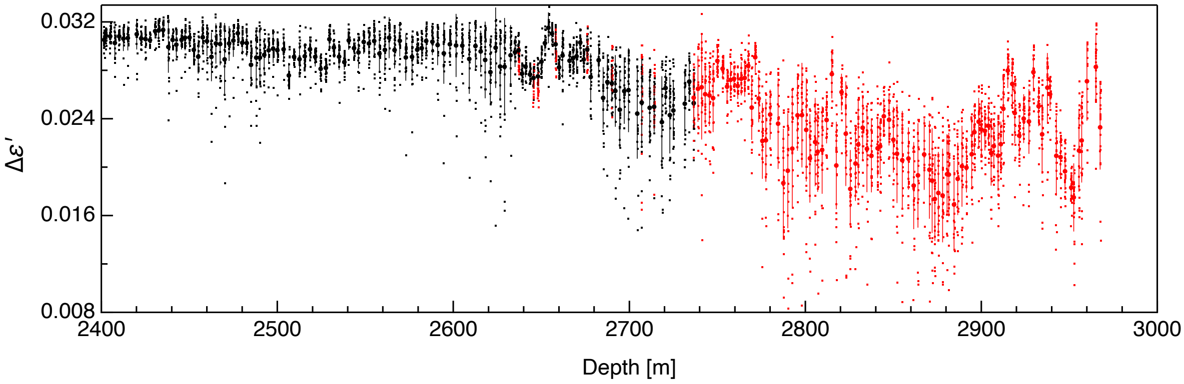

Figure 3. The $\Delta\varepsilon'$ measured along the DF2 ice core. Dots represent raw data, recorded at every 0.02-m step. Markers and bars indicate the average values and SDs for each 0.5-m step. Black and red markers/dots indicate data obtained without and with rotation of the samples in the open resonator, respectively (See Figures C1a and C1b in Appendix C), respectively.

4.2 COF from the Laue X-ray diffraction method

Figure 4 presents examples of the COF obtained through thin-section measurements. Examples from 15 of the 43 measured depths are shown. In the diagrams, red dots and dark blue dots represent the orientations of *c*-axis and *a*-axis within the space, respectively. The three panels, from left to right (views from 1 to 3), are as follows. View 1: Horizontal view from the axis of the microwave beam incidence (the center of the diagram), which is the same view as in Figure C1b in Appendix C, without information of the IACC or the HOCC. View 2: Horizontal view from the orthogonal direction (axis) of the IACC. This view is attained by horizontal rotation of the system using the vertical axis, by moving the center of the *c*-axes cluster to the periphery of the diagram. This operation relates to the HOCC. The center of the diagram is parallel to the girdle of the *a*-axes. This view corresponds to that in Figure C1b'. View 3: View seen from the center axis of the *c*-axes cluster. In all diagrams, green triangle markers indicate the orientation of the vertical in the ice sheet.

COFs generally exhibit a strong single-pole cluster. The strength of this cluster fluctuates with increasing depth. In contrast to observations in the UP80% (in Saruya et al., 2022b), the cluster strength becomes weaker at greater depths. Since each crystal grain of the hexagonal crystal lattice has three equivalent *a*-axes orthogonal to the *c*-axis, the distribution of the *a*-axes forms a girdle plane orthogonal to the *c*-axes cluster at each depth. The girdle appears to be nearly uniform. We could not find a clustering or anisotropy of *a*-axes below 2400 m. As for the IACC, it is monotonically larger at greater depths down to 2967 m. Figures 4(k–o) display data from the deepest five depths, which lie within the bottom 2% of the ice sheet. At each depth, red and blue number markers indicate the distributions of the *c*-axis and *a*-axis, respectively. Because of grain growth near the bed of the ice sheet, the largest number of crystal grains in a thin section was six. Therefore, the center of the clusters could not be determined with this very limited number of grains. In these five diagrams, we did not find any angular relations between neighboring grains. Both the IACC and the HOCC were extracted through the observation of COF, considering views from 1 to 3. Both were used for the corrections from $\Delta\varepsilon'$ to $\Delta\varepsilon$. We present correction procedures in Appendix D. Corrected $\Delta\varepsilon$ values are shown in Figure 5a. In addition, the MICC values were calculated using the thin-section-based COF data. Both the IACC and MICC values are presented in Figure 5c.

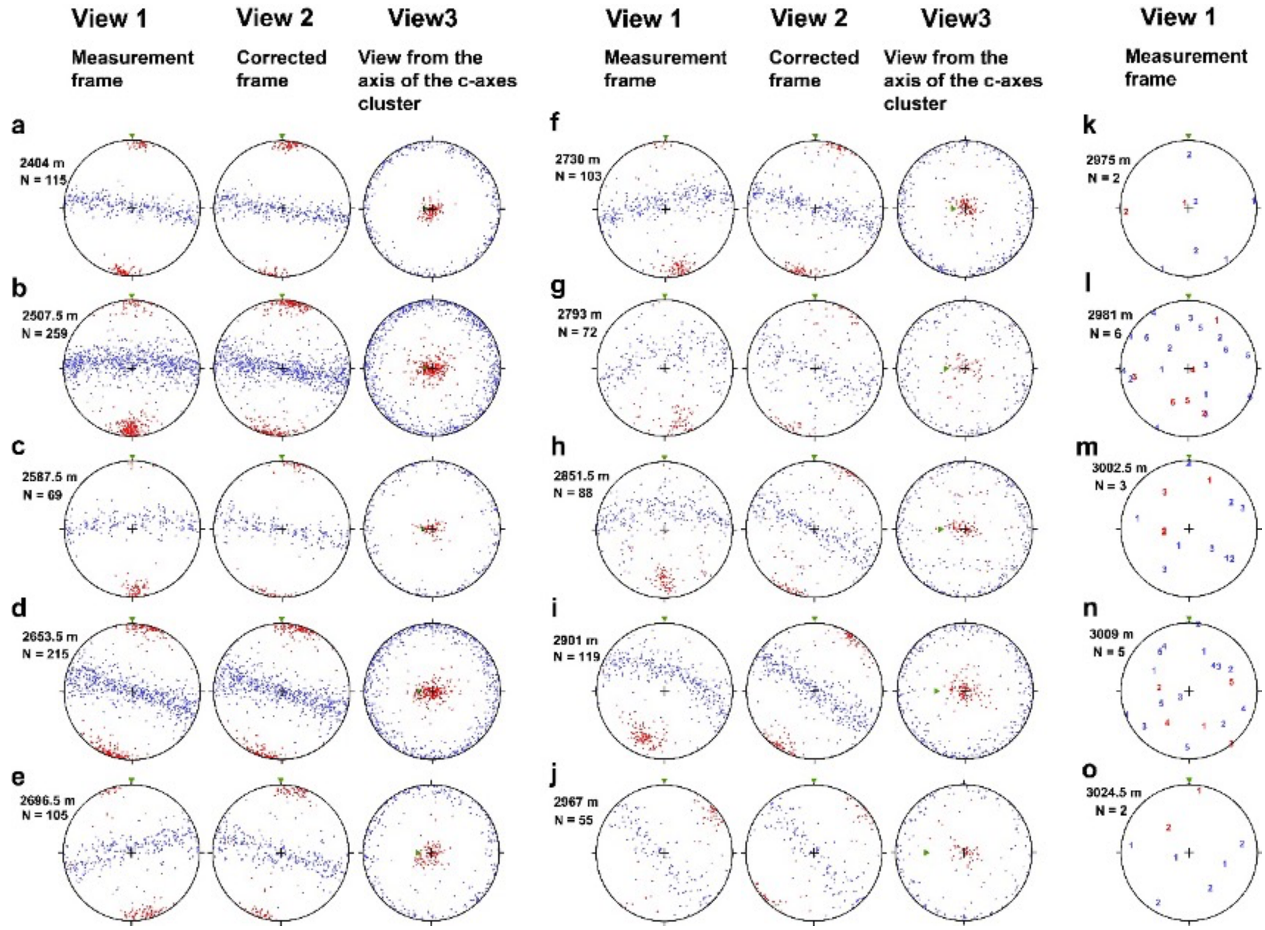

Figure 4. Examples of COF data obtained by the Laue X-ray diffraction measurements. 15 depths were selected from a total of 43. At each depth, red and blue colors for dots/markers represent the distributions of *c*-axis and *a*-axis, respectively, projected on a Schmidt equal area net diagram (e.g., Langway, 1958). Diagrams from (a) to (j) represent ten examples in depth range of 2400 and 2967 m. For these ten depths, the left diagram (view 1) is the projection from the measurement frame (refer to Figure C1b). Center diagram (view 2) is the projection from the corrected frame (see Figure C1b'). Right diagram (view 3) is the projection from the center of the *c*-axes cluster. Green triangles in each diagram indicate the vertical orientation in the ice sheet. The vertical orientation aligns with the core axis. Diagrams from (k) to (o) represent the deepest five depths, ranging from 2975 to 3024.5 m. Because of grain growth near the bed of the ice sheet, number of crystal grains in each thin section was less than 6. Instead of dots, number markers were used to indicate the orientation of each grain.

4.3 Variations in corrected $\Delta\varepsilon$ and SD values

The Panels in Figure 5 display a set of physical features. The $\Delta\varepsilon$ value (see Figures 5a) reaches approximately 0.031 at depth of 2430 and 2654 m. After reaching this maximum level, the $\Delta\varepsilon$ values decrease, accompanied by larger SD at greater depths (see Figures 5b). The decrease in $\Delta\varepsilon$ values and larger SD are directly linked to the scatter in each individual $\Delta\varepsilon$ measurements (represented by dots in Figure 5a). When scatter is pronounced, $\Delta\varepsilon$ value averaged over each 0.5-m segment becomes smaller and the SD larger. At depths greater than about 2900 m, the Δ*ε* values exhibit large fluctuations over distances on the order of 10 m. It is noted that when the SD values are large, each ice core displays numerous sharp negative spikes in Δ*ε*, as shown by the dots in the panel and an example profile in Figure E2.

4.4 Layer inclination and grain size

The results for the Inclination Angle of the Visible Layers (IAVL) and the grain sizes are presented in Figures 5c and 5d, respectively. The IVAL will not be exactly orthogonal to the IACC if simple shear strain occurs in the ice sheet. The simple shear in principle contains components of compression, extension, and rigid-body rotation of the system. In this case, an axis orthogonal to the shear plane and the IACC will deviate. Indeed, we observed that the IACC and the IVAL deviate over a wide range of depths, deeper than about 2580 m (Figure. 5c). The deviation is pronounced at depths between 2800 and 2900 m. We also note that the IVAL changes in stepwise manner at 2580 and 2770 m.

The grain size tends to be larger during interglacial-periods and smaller during glacial periods. We observed that the data points of Δ*ε*, the SD of Δ*ε,* and grain sizes are approximately synchronized, implying the presence of common underlying mechanisms. In grain sizes we could observe only weak increasing trend versus depth. The grain sizes at depths between 2900 and 2950 m remain small despite temperatures higher than –5 °C. At depths greater than 2950 m (in the deepest approximately 2%), the grain sizes become extremely large.

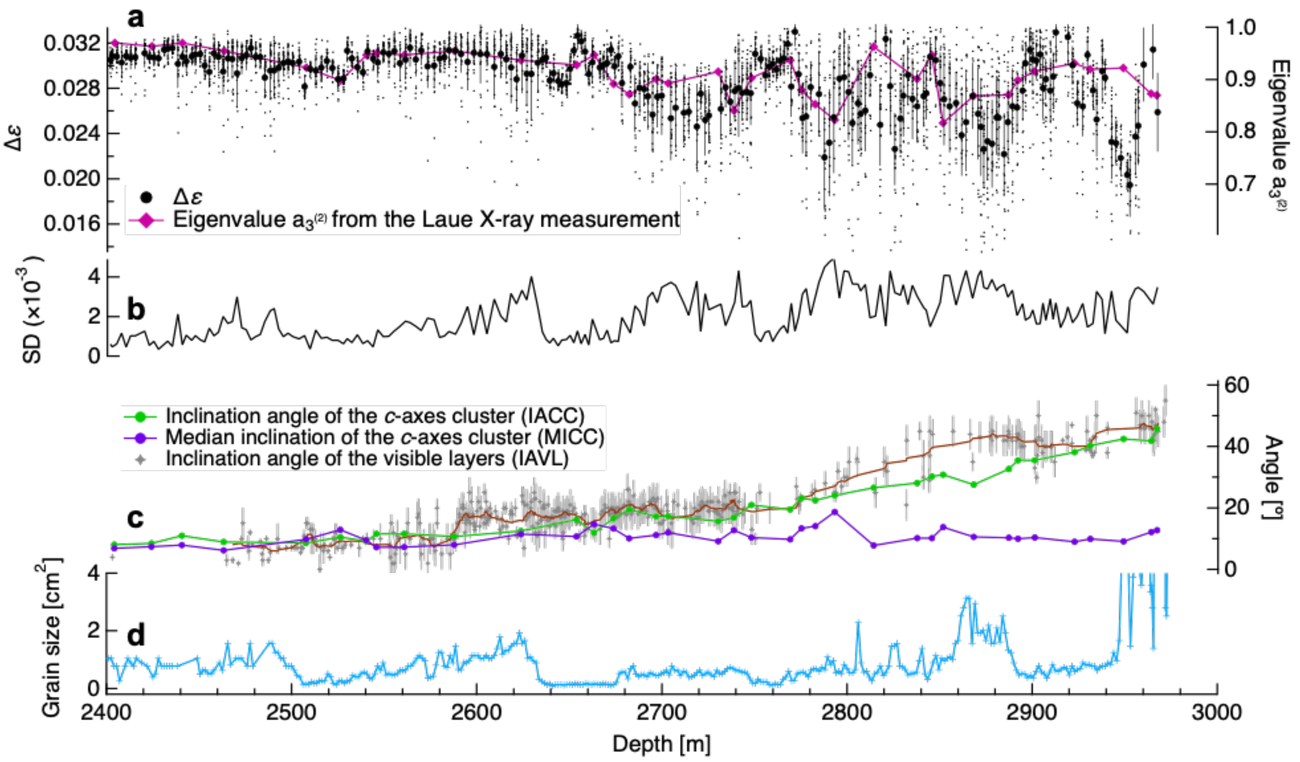

Figure 5. Comparison of $\Delta\varepsilon$ with various data in the LO20%. (a) $\Delta\varepsilon$ presented as raw data (dots) and as mean values for each 0.5-m segment (black markers) with the SD (bars). Light purple markers indicate values obtained with thin-section-methods. The right axis provides a scale for eigenvalue $a_3^{(2)}$. (b) SD for $\Delta\varepsilon$. (c) IACC (green lines and markers), IAVL (the inclination angle of the visible layers) (gray markers and bars) with moving average over 10 measured points (brown profile), and MICC (Median Inclination of *c*-axes with reference to the axis of the *c*-axes Cluster) (purple profile). (d) Grain size.

4.5 Microstructural features

Examples of microstructures are presented in Figure 6. Five examples include impure ice (panel a: 2648 m, ~270 ppbv dust concentration; panel c: 2759 m, ~137 ppbv), less impure ice (panel b: 2685 m, ~10 ppbv; panel d: 2872 m, ~3 ppbv), and impure deep ice (panel e: 2909 m, ~80 ppbv). Here, we use the term impure to mean that ice contains either insoluble particles (like dust) or soluble impurities such as dissolved ionic species. It is noteworthy that the concentration of the less impure ice is markedly smaller than in impure ice. We provide polarized images, COF data of each grain obtained by G50, and microstructures. Black solid lines indicate GBs. GBs on the reverse side of a thin section are visible as thin lines. The legend for COF data is by lower circle. The color of each grain indicates the direction of *c*-axis orientation. The red color corresponds to the vertical direction. Therefore, *c*-axis of red color grain is orientated toward the vertical direction. The crystal grains in the impure layer (panels a and c) represent the inclined layer and elongated shape. These features were not observed at less impure depths. The subgrain boundaries (hereinafter sGBs) in the impure layer look straight, parallel to the major axis of the grain shape (shown by black arrows). In contrast, sGBs in the less impure ice are complicated (panel b). The GBs exhibit a convex shape toward the complex sGBs in adjacent grain (indicated by gray arrows). Usually, a feature of this kind is produced by “migration recrystallization” (Faria et al., 2014b). At panel d, we observe many grains with *c*-axis orientation greatly offset from the vertical direction. In the two deepest samples (panels d and e), the GBs are quite straight and there are few sGBs. Panel (e) was a sample of impure layers; however, we could not find features of impure layers (brick-wall pattern like panel a and b). Detailed microstructures are shown in Figure 11. An example comparing $\Delta\varepsilon$ values with microstructure derived from thin-section measurement is provided in Appendix E. Since the $\Delta\varepsilon$ values are volume-weighted averages within the microwave beam, mean $\Delta\varepsilon$ value within a 0.5 m core sample decreases when there are sharp drops of $\Delta\varepsilon$ associated with *c*-axis orientation distinctly offset from surrounding grains.

https://doi.org/10.5194/egusphere-2023-3146
Preprint. Discussion started: 5 January 2024

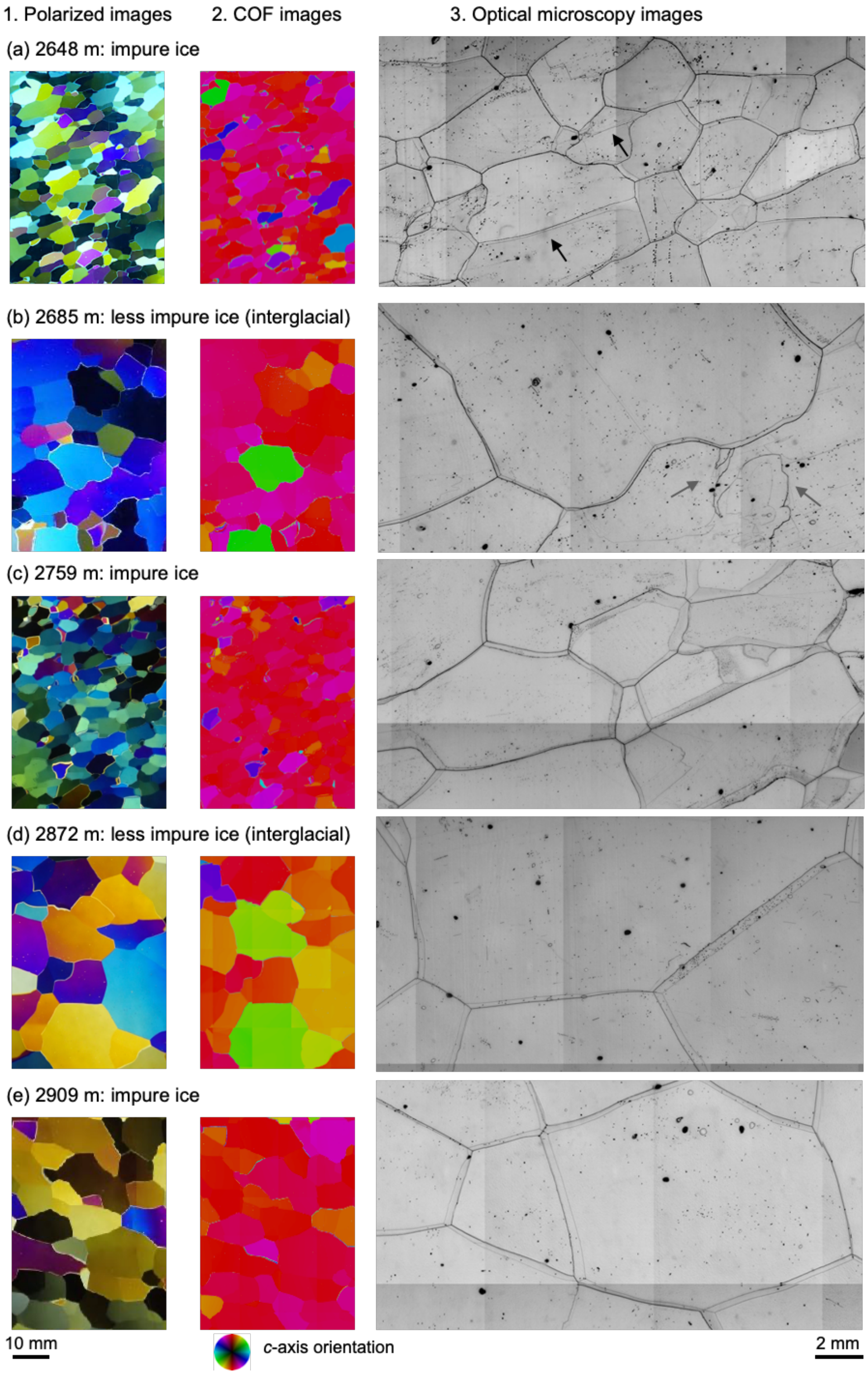

Figure 6. Microstructure images representing typical examples from five depths. Depths and types of ice are specified in the figure. For each depth, a polarized image (left), a COF image (center) and optical microscopy images (right) are presented. Black solid lines indicate GBs. GBs on the reverse site of a thin section are visible as thin lines. Arrows in panels (a) and (b) indicate subgrain boundaries (sGBs). The legend for COF images is shown at the bottom. The color of each grain indicates the orientation of *c*-axis. Red color corresponds to the vertical direction.

5. Discussions

5.1 COF development

5.1.1 Depth-dependent variations of $\Delta\varepsilon$ in the entire core

Figure 7 presents $\Delta\varepsilon$, its SD, and detrended $\Delta\varepsilon$ values across the entire thickness of the core. In the UP80%, $\Delta\varepsilon$ increased with increasing depth and reached the possible maximum level at the bottom of the UP80%. Below this, we observe that the zone between approximately 2400 and 2650 m is where the trend of $\Delta\varepsilon$ variation changes. The $\Delta\varepsilon$ values began to show larger fluctuations with numerous sharp drops in individual $\Delta\varepsilon$ data points. We suggest that these changes indicate a transition in the physical mechanisms responsible for deformation. Saruya et al. (2022b) argued that the linear trend of $\Delta\varepsilon$ in the UP80% was dominated by dislocation creep. A $\Delta\varepsilon$ value of about 0.031 implies that it is close to the $\Delta\varepsilon$ of a single crystal (0.0334 ± 0.0007 at –30 °C; Saruya et al., 2022b). The state of the COF cluster with this $\Delta\varepsilon$ of about 0.031 is equivalent to the normalized eigenvalue $a_3^{(2)}$ of about 0.93 for a single pole COF. On one hand, it is well-known that ice with a single-pole fabric is resistant to strain in uniaxial compression axis configurations, as the basal planes of hexagonal ice have no room to slip for further strain. On the other hand, it is also evident that ice, even in the LO20%, continues to deform, as shown by analyses of thinning functions (e.g., DFICPM, 2017). The question then arises: What mechanisms dominate further deformation? We suggest three possibilities for mechanisms: (i) dominance of dislocation creep using slip systems other than basal plane slip within the hexagonal ice, (ii) dominance of diffusional creep, and/or (iii) dynamic recrystallization. These mechanisms can cause further deformation in ice with highly clustered COF. The first possibility is unlikely because it assumes extremely hard ice within the ice sheet, which does not align with the data. The second is also unlikely under a condition where we observe drastic changes of COF. In contrast, what we observe in the data is evident occurrence of dynamic recrystallization, typical for warmer ice, and continuation of dislocation creep using the slip system of the basal planes of hexagonal ice for grains that arise through recrystallization. We suggest that evidence includes a wide scatter of dots with low values of $\Delta\varepsilon$ in figures, leading to smaller average $\Delta\varepsilon$ values in interglacial periods, accompanied by large SD values. We interpret the wide scatter as indicative of grain nucleation and subsequent growth.

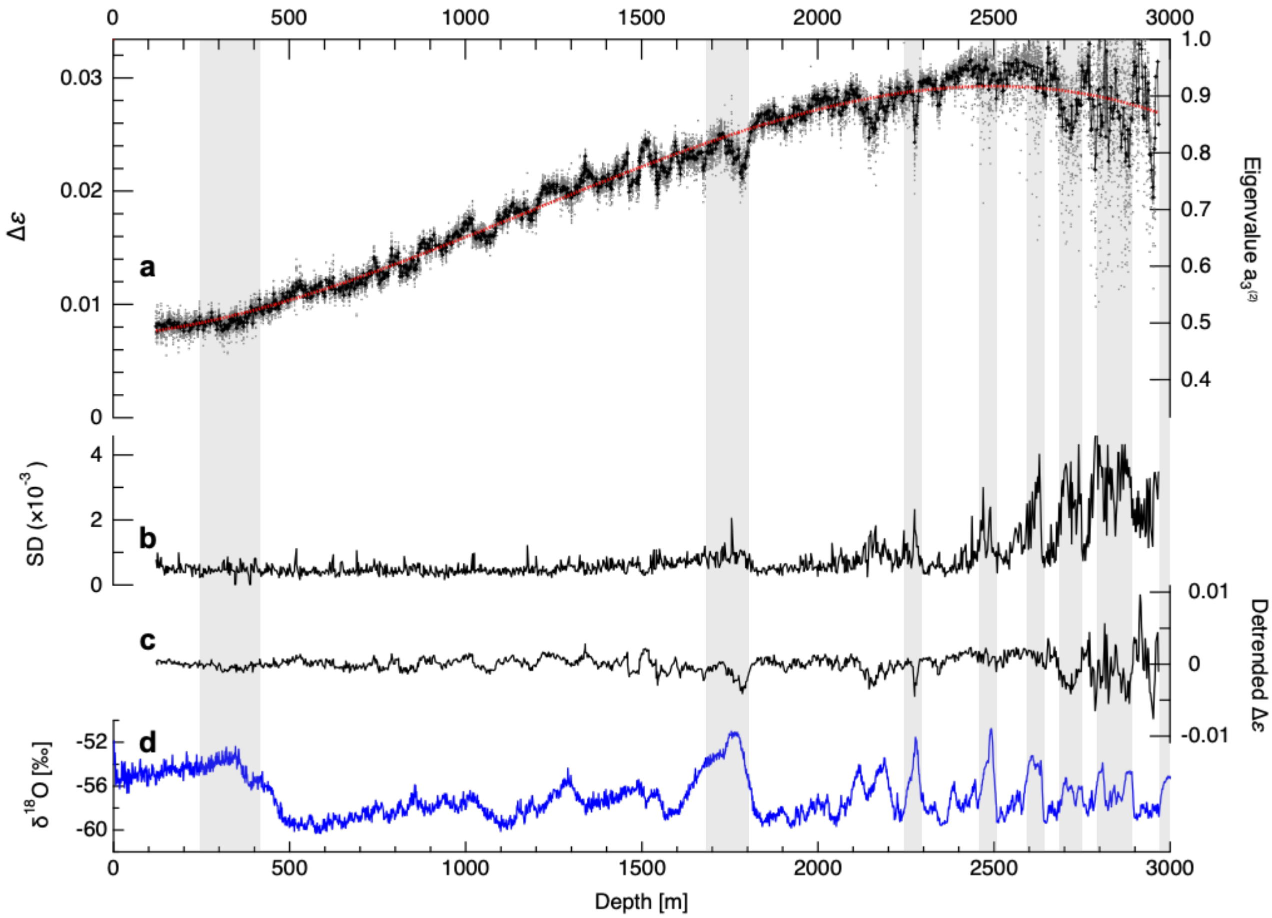

Figure 7. Variation of the Δ*ε* and its SD across the entire depths of the core. (a) Δ*ε* presented as raw data (dots) and mean values for each 0.5-m segment (black markers). The red dashed line indicates a third-order fitting. Dots represent Δ*ε* values at every 0.02-m step. Data for the UP80% are from Saruya et al., 2022b. (b) The SD for Δ*ε* values. (c) Detrended Δ*ε* values, defined as deviations from the third-order fit to the data in panel (a). (d) Oxygen isotope ratios ($\delta^{18}O$) in the DF ice cores, modified from DFICPM, 2017. Gray shading highlights the approximate depths of interglacial periods.

5.1.2 Comparison of microstructures and COF at deeper part of three summit ice cores

We first compare COF data from DF with that of EDC, representing two dome summits in Antarctica, separated by approximately 2000 km. It is notable that these two sites are similar in terms of glaciological conditions, including surface temperature, annual mean surface mass balance and ice thickness (see Table 3). Figure 8a indicates the relationship between Δ*ε* value and normalized eigenvalue $a_3^{(2)}$ which can be expressed as $a_3^{(2)} = (2\Delta\varepsilon / \Delta\varepsilon_s + 1) / 3$, assuming a single-pole COF without horizontal anisotropy. Here, $\Delta\varepsilon_s$ represents the dielectric anisotropy of a single crystal. In the figure, we can observe the scatter of dots for the DF ice core. General trends in cluster strength and grain size are very similar in both ice cores across all age scales. Note that the sampling volume differs by a factor of 10^2 for each single data point between the thick-section-based DF data and the thin-section-based EDC data (Saruya et al., 2022b). In the bottom part of the EDC core, there is a correlation between the grain size and impurity concentration (Durand et al., 2009). However, no clear correlation between the COF and climate or chemical properties was reported. Another relevant observation is that Durand et al. (2009) pointed out depth-dependent developments in COF clustering are similar in the GRIP Greenland dome summit ice core (Thorsteinsson et al., 1997) and EDC core in Antarctica. Indeed, at the three summit sites, the depth zones where the maximum clustering appears are similar (see Table 3). The similarity among these three sites across both hemispheres implies that certain physical mechanisms are driving this similar development of COF. We speculate that temperature profiles are primarily related to control enhancement of molecular diffusions and dislocation creep. However, two Antarctic sites (DF and EDC) and the GRIP site have significantly different temperature conditions; the Antarctic sites are much colder at the surface and warmer near the bed compared to GRIP (see data in Table 3). Thus, the similarity of depth zones for maximum clustering may be more related to the total amount of strain, regardless of the temperature difference by about 10°C in the LO20% (see Table 3). In this hypothesis, at the bottom of the UP80%, the thickness of ice is approximately 10% of the original ice equivalent thickness at the time of deposition (Figure 9f). At this depth, the eigenvalue $a_3^{(2)}$ reaches about 0.93. This state of saturation of the *c*-axis cluster may be more effective as a condition to trigger active emergence of recrystallization.

An implication for this similar COF development is rheology of the ice sheet. The deepest 10–20% of the polar ice sheets are typically characterized by their ability to easily deform under horizontal shear, due to high temperatures and well-clustered COF. Within this thickness, the clustering strength of the *c*-axes along vertical fluctuated in these ice cores. Thorsteinsson et al. (1997) suggested that migration recrystallization might be the cause of COF fluctuations in the deepest part of the GRIP core, although direct evidence was not observed. Migration recrystallization occurs when the temperature is close to melting point (e.g., De La Chapelle et al., 1998; Humphreys and Hatherly, 2004) and the driving force for GB migration is stored, which is achieved in the very deep parts of ice sheets. We observed evident features indicating the occurrence of migration recrystallization (see Section 4.5 and Figure 6). These features imply presence of stored strain energy which induces the migration recrystallization (Faria et al., 2014b). We therefore suggest that migration recrystallization predominantly occurs at the dome summits of both ice sheets.

Table 3: Environment of the DF, EDC, and GRIP sites

Site	Elevation (m)	Ice thickness (m)	Annual mean SMB (kg m^{-2} y^{-1})	Annual mean surface air temperature (°C)	Depth of temperature at –10 °C (m)	Depth of maximum COF cluster and corresponding temperature range (°C)	References

DF	3810	3028 (±15)	24–28	–54.4	ca. 2700	2400–2650 from –18 to –12	This study, DFICPM, 2017, Oyabu et al., 2023, Yamanouchi et al., 2003
EDC	3233	3273 (±5)	25	–54.5	ca. 2800	2400–2650 from –20 to –13	EPICA Community Members, 2004, Durand et al., 2009, Buizert et al., 2021
GRIP	3216	3085	230	–30.0	ca. 2960	2600 –28	Dahl-Jensen, et al., 1993, 1998, Thorsteinsson et al., 1997

https://doi.org/10.5194/egusphere-2023-3146
Preprint. Discussion started: 5 January 2024

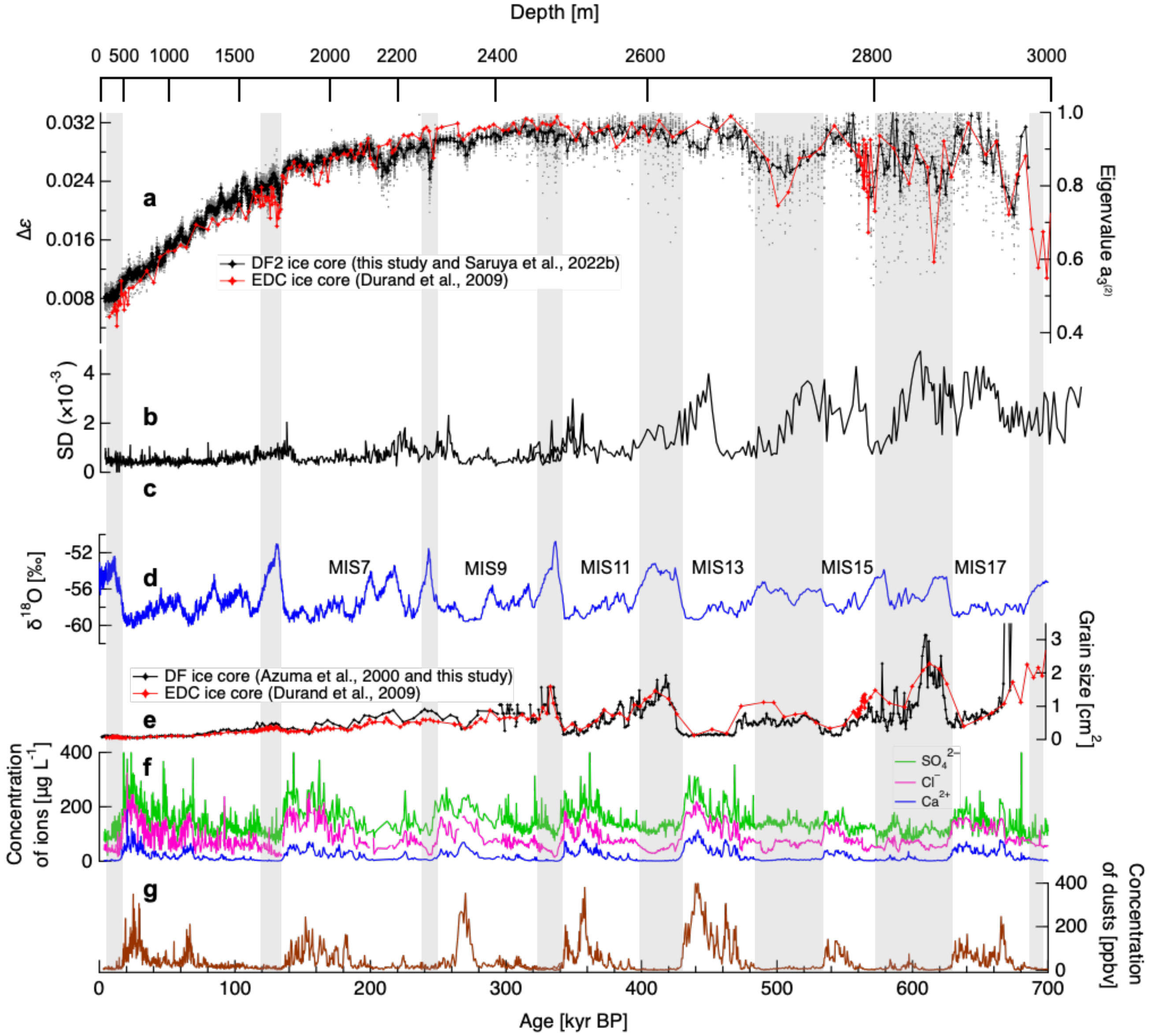

Figure 8. COF data from the DF core and the EDC core are compared using common age scales. Here, we applied the DF2021 age scale (Oyabu et al., 2022) for ages younger than 216 thousand years BP and the AICC2012 age scale (Bazin et al., 2013) for older ages. Light-gray shading indicates the interglacial periods. (a) $\Delta\varepsilon$ presented as raw data (dots) and as mean values for each 0.5-m segment (black markers for DF) or for each thin section (red marker for EDC). The right axis provides a scale for normalized eigenvalues. (b) SD for $\Delta\varepsilon$ in the DF core. (c) Detrended $\Delta\varepsilon$ values in the DF core. (d) Oxygen isotope ratios ($\delta^{18}O$) in the DF ice core. (e) Grain size in the DF cores (Azuma et al., 2000 and this study) and the EDC core (Durand et al., 2009). (f) Concentrations of Cl^-, SO_4^{2-}, and Ca^{2+} ions (Goto-Azuma et al., 2019). (g) Concentration of dust particles (DFICPM, 2017).

5.2 Variations in the layer structures in the deeper part

5.2.1 Temperature and stress conditions

In ice physics, it is well-accepted that both plastic deformation and the molecular diffusion process in ice are highly temperature-dependent (e.g., Petrenko and Whitworth, 1999). The conditions of ice sheets in Antarctica, in terms of temperature and stress, are located on a boundary zone between dislocation and diffusional creep on the deformation mechanism map (e.g., Shoji and Higashi, 1978; Goodman et al., 1981). When ice is under temperatures close to the melting point in the LO20%, its viscosity is lower, and diffusion coefficients are higher compared to the colder ice in the upper layers (from –20 to –55 °C in the UP80%) by a factor of 10 to 10^2 (e.g., Petrenko and Whitworth, 1999). The recrystallization processes require thermally activated molecular diffusion; this condition exists in very deep ice. Regarding the stress field, the coring site is situated on a bank very close to a subglacial trench (Figure 1c). Between the trench and the coring site, the depth difference and distance are approximately 100 m each. This geometry corresponds with the maximum IACC (approximately 45 degrees) and the IAVL (approximately 45 degrees) near the base of the ice sheet (Figure 5c). In addition, the deeper trench may act as pathway for flow of subglacial water and the deeper bed is a location for more melt (e.g., Pattyn, 2010, Fujita et al., 2012). Thus, we hypothesize that there is a shear strain component directed towards the subglacial trench. The rheology of polycrystalline ice with a single-pole fabric is like that of the single crystal. It easily deforms under shear stress. We suggest that the shear stress dominates the deformation of ice at the bottom part of DF.

5.2.2 Relationships between the COF and layer structure parameters

Figure 9 illustrates the relationships between COF, layered structures, and physicochemical properties. The figure plots $\Delta\varepsilon$ (mean and raw data from DTM), eigenvalues (from the Laue X-ray diffraction method), SD values, the distribution of *c*-axes relative to a plane orthogonal to the *c*-axes cluster, grain sizes, IACC, IAVL, MICC, the annual layer thickness-thinning function, $\delta^{18}O$, concentrations of Cl^-, SO_4^{2-} and Ca^{2+} ions, and concentration of dust particles. The relationship between COF and layered structures evolves with increasing depth (Figures 9a–9f). The angles of IAVL and IACC are approximately consistent at depths shallower than about 2600 m (Figure 9e). This indicates that the system, composed of visible layers and the *c*-axes cluster, rotated together as a rigid body. At depths deeper than about 2600 m, the consistency of the angle in IAVL and IACC depends on glacial/interglacial periods. In glacial periods (MIS13, MIS15, and MIS17), both angles are approximately consistent, whereas in interglacial periods (MIS12, MIS14 and MIS16), they are not; the IACC is smaller than IAVL. This implies that the crystal grains undergo a simple shear mechanism, rotating less than layer structure rotation in these depth ranges, particularly during interglacial periods. In principle, simple shear is a superposition of pure shear and the rigid-body rotation of the system. Schematic diagrams of the relationships between layered structures and orientation of *c*-axes cluster are shown in Figures 10(a–c). The layer inclination is simply caused by the system's rigid-body rotation. The *c*-axes also fall within the system's rigid-body rotation. However, the cluster of the *c*-axes alone will rotate backward due to the compression components within the pure shear by dislocation creep. Thus, the inconsistency of the angles is the circumstantial evidence for dominance of the simple shear at this depth range. Such features were not observed in the EDC ice core. This suggests that these features are due to an environment specific to DF. In terms of the distribution of *c*-axes (Figure 9c), we can find crystal grains with *c*-axis oriented around 30–60 degrees at depths below 2600 m. It is believed that new grains tend to form with an orientation favorable for basal glide (Cuffey and Paterson, 2010), that is, approximately 45 degrees from compressional axis. We suggest that grains with a *c*-axis orientation of around 30–60 degrees represent nucleated grains in the deeper part, and that these grains might grow and eliminate old grains by migration recrystallization. Such a process results in significant COF changes and more occurrence of shear by dislocation creep. We discuss the details of recrystallization process in Section 5.3 in terms of microstructure.

Next, we discuss layer thinning. DFICPM (2017) analyzed thinning function (the ratio of an ice layer thickness to its initial thickness at the surface) of the DF2 core from depth sequence of the climate signals and annual layer thickness (see Figure 9f). The thinning function decreased to a local minimum at about 2750 m and then increased again towards greater depths. The authors hypothesized that spatially inhomogeneous basal melting might be linked to this anomalous thinning. In Figure 9f, the broad local minimum of the thinning function is located at 2700–2800 m. This depth range agrees well with starting depths for large inconsistency between the IACC and the IVAL in MIS16. Importantly, this depth is an approximate boundary where larger fluctuation of the $\Delta\varepsilon$ started. In addition, both the IACC and the IAVL have features of upward inflection at this depth range of glacial period of MIS 15. We speculate that the observed phenomena were caused by higher temperatures, the activated occurrence of recrystallization, and increased strain of simple shear from the bed. Then, we propose a scenario for development of the layer structure at the deeper part in Dome Fuji based on the observed data using Figure 10d. An important point is that the DF drilling site is located just above a subglacial slope at the bank of the drainage pathway of the meltwater (Figure 1c in this paper and Figure 8d in Tsutaki et al., 2022). Under the dominance of the vertical normal stress near the dome, horizontal shear appears mainly on subglacial slopes rather than ridges or troughs (Tsutaki et al., 2022). Basal troughs are often influenced by basal melt or connected to deeper troughs of more basal melt. Consequently, troughs tend to serve as rapid pathways for ice flow. Thus, we suggest that the subglacial slope near the trough causes ice to flow towards the center of the trough, disturbing the layered conditions. Furthermore, spatially inhomogeneous basal mass loss due to melting lead to an imbalance of force equilibrium in the vertical direction. Below the hardest ice in the transition zone, ice mass is lost locally at the base. As a result, layers can be stretched downwards, creating a convex shape centered around the location of the trough.

https://doi.org/10.5194/egusphere-2023-3146
Preprint. Discussion started: 5 January 2024

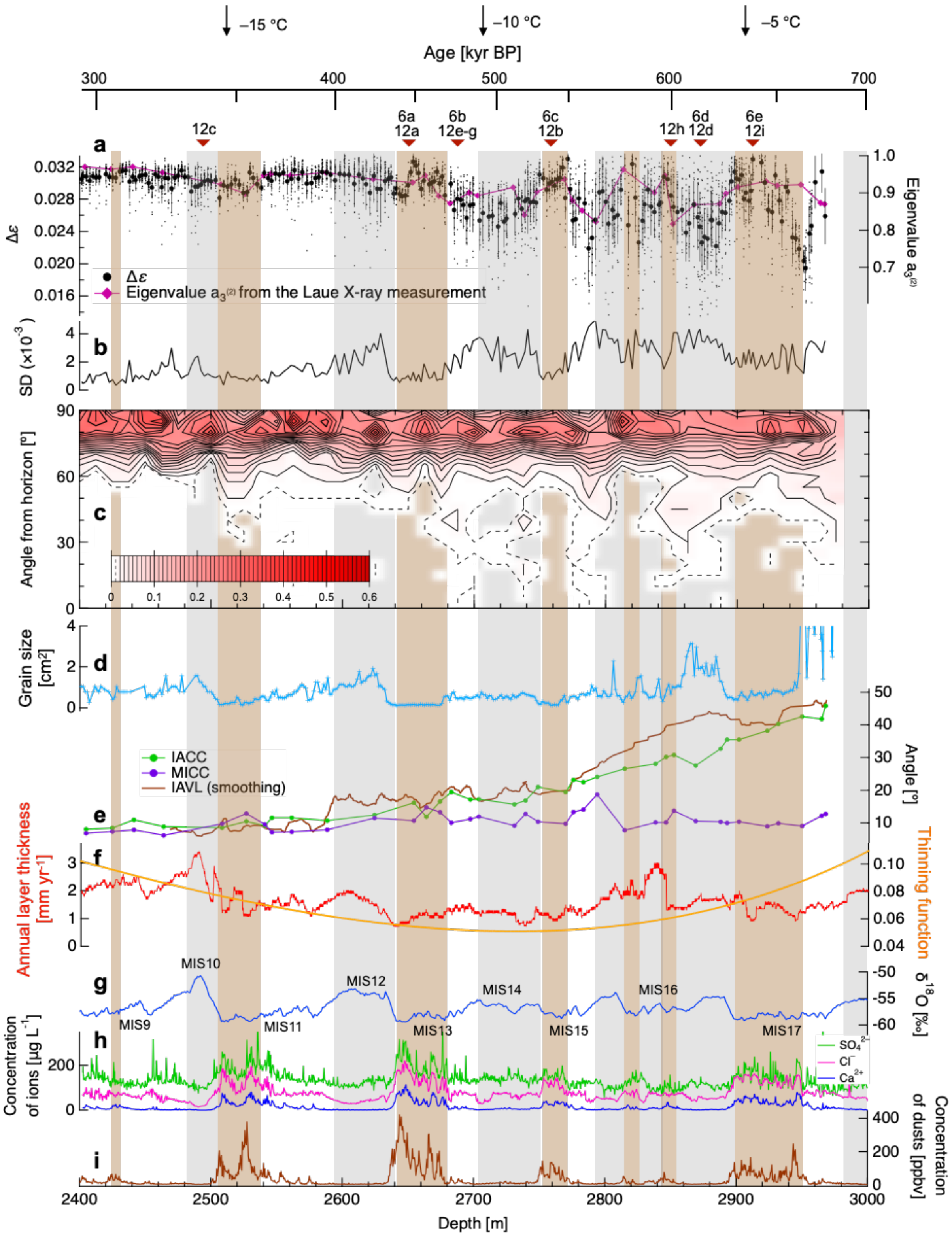

Figure 9. Detailed view of the comparison of $\Delta\varepsilon$ with various ice core data in the LO20%. (a) $\Delta\varepsilon$ (mean and raw data from DTM) and eigenvalues (from the Laue X-ray diffraction method) (b) SD. (c) Distribution of *c*-axes as angles from a plane orthogonal to the cluster of *c*-axes. This was analyzed using the data from the Laue X-ray diffraction method. The probability of the presence of *c*-axes is expressed with contour lines. (d) Grain size. (e) IACC, MICC, and IVAL (smoothing). (f) Annual layer thickness and thinning function (DFICPM, 2017), (g) $\delta^{18}O$ (DFICPM, 2017). (h) concentrations of Cl^-, SO_4^{2-} and Ca^{2+} ions (Goto-Azuma et al., 2019), and (i) concentration of dust particles (DFICPM, 2017). Gray and brown shading indicate interglacial periods and depths with a higher concentration of dust particles (representing impure layers), respectively. Representative borehole temperatures are shown in the upper side (from Motoyama et al., 2020). The depths at which we observed the microstructure are indicated in the upper part.

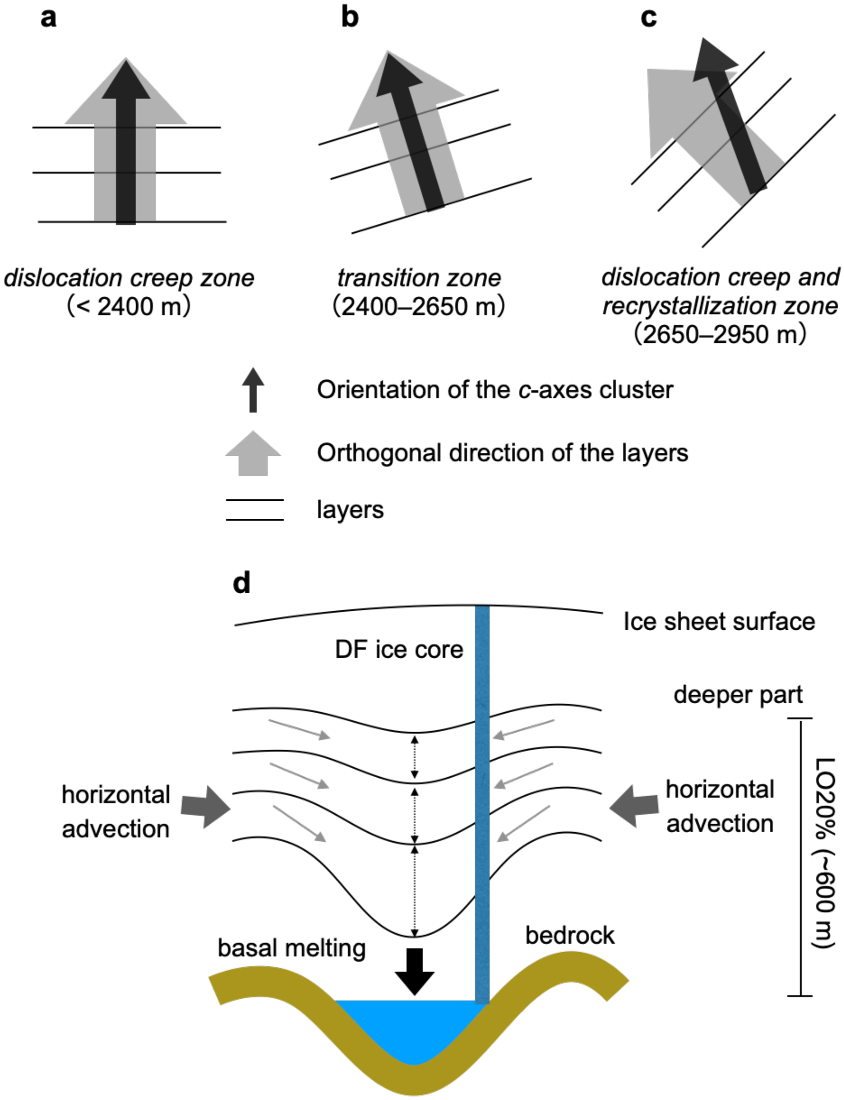

Figure 10. Schematic diagram of layered structures at Dome Fuji. (a–c) Diagram illustrating the relationship between layers and the orientation of the *c*-axes cluster. Refer to the main text (Section 5.4) for zoning details. (a) Far above the bedrock, layers and the orientation

of the *c*-axes are consistent, both oriented vertically. (b) Up to a depth of 2650 m, layers and the *c*-axes cluster rotate together as a rigid body. The directions of *c*-axis clustering and layers are consistent, yet they deviate from the vertical. (c) In addition to the rigid body rotation of the system, the cluster of *c*-axes rotates backward due to the compression component of pure shear. The orientations of the *c*-axes clustering and layers diverge. (d) The DF drilling site is located just above the subglacial slope at the bank (see Figure 1c), and horizontal shear along subglacial slopes appears near the trough. We suggest that the subglacial slope induces ice flow towards the center of the trough. Spatially inhomogeneous mass loss due to basal melting can lead to an imbalance in force equilibrium in the vertical direction. Layers can stretch downward, forming convex shape centered around the trough.

5.2.3 Relationships between COF with ionic impurities and dust concentrations

Within the UP80%, Saruya et al. (2022b) investigated the controlling factors of COF by comparing $\Delta\varepsilon$ with various ionic impurities and dust concentrations. They found that $\Delta\varepsilon$ is correlated positively with the concentration of Cl^- ions and inversely with the amount of dust particles; the correlation grows markedly in a range from MIS5 to MIS8. For the depths of the LO20%, we also compared $\Delta\varepsilon$ with $\delta^{18}O$, grain size, concentrations of ionic impurities (Cl^-, SO_4^{2-} and Ca^{2+}), and dust particles (Figure 9). These ions were sometimes examined in terms of deformation enhancement (e.g., Nakamura and Jones, 1970; Freitag et al., 2013; Hammonds and Baker, 2018). Referring to the $\delta^{18}O$ profile, we observe that depressions in the mean $\Delta\varepsilon$ (caused by a large scatter of data points) occur during interglacial periods at depths below 2650 m; the depressions deepen with larger scatter of the raw data at greater depths. The relative sizes of SDs are smaller in glacial periods and larger in interglacial periods, respectively (Figures 9a, 9b and 9g).

As for the ionic impurities we investigated, only Cl^- ions have a property to be easily substituted for the location of H_2O molecules in the ice crystal lattice (Jones, 1967; Jones and Glen, 1969; Nakamura and Jones, 1970). Dissolved and substituted Cl^- ions can increase density of the point defects in ice and promote dislocation movement, which will result in enhanced plastic deformation. Another characteristic of the Cl^- ions is their ability to be easily homogenized by diffusion through the ice lattice (e.g., Thibert and Domine 1997, Barnes et al., 2003, Fujita et al., 2016). Therefore, the influence of Cl^- ions on the deformation will be smoothed out and occurs in wider depths with time. In contrast to the softening effects of dissolved Cl^- ions, dust particles are suggested to impede COF changes and thus deformation (Saruya et al., 2022b). The influence of dust particles on impeding deformation will remain since the dust particles do not diffuse easily. In our data from the LO20%, the relationship between $\Delta\varepsilon$ and Cl^- ions is unclear. That is, even at depths where the concentration of Cl^- ions is high, we did not find stronger *c*-axes cluster. In contrast, the highly concentrated dust particles had an apparent influence on the $\Delta\varepsilon$ values, maintaining a persistently high level of $\Delta\varepsilon$ below 2600 m (Figure 9a).

As for the influence of dust particles on the deformation regime, Saruya et al. (2022b) suggested two possibilities: (i) restricted deformation due to the inhibition of dislocation by dust particles and/or (ii) the contribution of diffusion creep that does not cause *c*-axis rotation because, with this mechanism, only molecules diffuse due to the condition of smaller grains. In the former case, the smaller $\Delta\varepsilon$ values can be explained as a result of weaker clustering of *c*-axes due to restricted deformation. In the latter case, the smaller $\Delta\varepsilon$ values are also explainable as a result of the contribution of diffusion creep instead of

https://doi.org/10.5194/egusphere-2023-3146
Preprint. Discussion started: 5 January 2024

dislocation creep. Even if ice is deformed significantly, diffusion creep does not leave any traces in the *c*-axis clustering. Which effect ((i) or (ii)) is more dominant remains unresolved. However, in either case, they can restrict changes in *c*-axis clustering. What we observed in ice below about 2600 m is that the degree of *c*-axis clustering in the dusty (i.e., impure) layers is stronger than in the surrounding layers. We suggest that these two unresolved mechanisms, related to restricted changes in the *c*-axes cluster, persist at depths below 2600 m, and that, in addition, dust particles have a strong influence on the occurrence frequency of dynamic recrystallization under higher temperature conditions in the LO20%.

To further explore the relationship of COF with ionic impurities, dust concentrations, and grain size, correlation coefficients (r) and p-values between them are given in Table 4. We analyzed each coefficient from data at 2.5 m intervals between 2400 and 2957 m (n = 216) with data smoothing at 2.5 m intervals for the concentration of Cl^- ions, dust particles, and grain size. We found that SD is negatively correlated with Cl^- ion and dust particle concentrations and positively with grain sizes. This implies that fluctuations of COF depend on these parameters. Details about this dependence are discussed in the next subsection (5.2.4). We also find, in contrast, that $\Delta\varepsilon$ is only weakly correlated with Cl^- and dust particle concentrations. Observing the brown shades in Figure 9, the variations of $\Delta\varepsilon$ values are apparently related to variations in dust particle concentrations in the impure layer below 2600 m. However, these variations are apparently unrelated in less impure layers. We suggest that this situation caused only weak correlations of $\Delta\varepsilon$ with Cl^- and dust particles. Interestingly, we find that grain size is clearly correlated with $\Delta\varepsilon$ and its SD. The development of COF is associated with recrystallization and grain growth, processes that are discussed in Section 5.3.

In addition to the Cl^- ions dissolved in ice and dust particles, as discussed above, we suggest that salt particles potentially influence COF development. Salt particles are known to exist solidly in ice cores at a volume fraction much larger than dust particles (Ohno et al., 2005). Depending on the type of salt particles, they have various eutectic points in the ice sheet. If the temperature condition is above each eutectic point, ions including Cl^- ions can be dissolved in the polycrystalline ice. However, we could not find any anomalous features in the data indicating the presence of additional COF changes. The phenomena seem complicated; little is known about the influence of salt particles or dissolved ions above eutectic points on deformation and microstructures.

Comparing the relationship of COF with ionic impurities and dust concentrations in the UP80% with the LO20%, in the UP80%, more/less impure layers have smaller/larger $\Delta\varepsilon$ values. In the LO20%, some thickness between 2400 m and 2650 m is a kind of transition zone; in it we find no clear correlation between $\Delta\varepsilon$ values and impurity. Below depths of about 2650 m, the trend is seemingly reversed. The COF clustering strength exhibited substantial fluctuations. There, more impure layers maintain clustering persistently. In less impure layers, relaxation of the COF clustering occurred, as represented by numerous negative spikes of $\Delta\varepsilon$ as we discussed in Section 5.1.1.

Here, crystal grain size provides additional information regarding impurity. Grain sizes in ice sheets generally increase over time by thermodynamic process (e.g., Cuffey and Patterson, 2010). This implies that the grain sizes increase towards greater depths until nucleation mechanisms commence. However, grain sizes in DF (and EDC) ice have fluctuations along depths. Azuma et al. (1999, 2000) reported that the grain sizes in the DF1 ice core in the UP80% is correlated with $\delta^{18}O$

variation and concentration of impurities, which was confirmed in this study (Figures 5 and 9). The same trend is common in the GRIP and Vostok ice cores (Lipenkov et al., 1989; Thorsteinsson et al., 1997). Thus, we can hypothesize that the physical phenomena (grain growth, nucleation, and recrystallization) determined by deposition of impurities are common across a wide area of the ice sheet. This situation closely aligns with our suggestion that the COF profile is basically similar across a wide area of the ice sheet, primarily due to the deposition of impurities. The COF contains information on several factors: (i) deformational history, (ii) grain growth, and (iii) recrystallization (e.g., Cuffey and Paterson, 2010; Faria et al., 2014a, b). Ultimately, all these factors are sensitive to the deposition of impurities. Impurities restrict grain boundary migration through drag and Zener pinning mechanisms and also impede dislocation movement (Alley and Woods, 1996; Durand et al., 2006). These characteristics result in slow growth of COF clustering in impure layers within the UP80% and slow relaxation of COF clustering in the LO20%. This leads to an apparent reversed correlation between $\Delta\varepsilon$ values and impurity levels in both the UP80% and the LO20%.

Table 4: Correlation coefficient (r) and p-values between each parameter in the LO20%. Correlation coefficients of >0.4 are shown in bold.

	$\Delta\varepsilon$		SD		detrended $\Delta\varepsilon$	
	r	p	r	p	r	p
concentration of Cl^- ions	0.19	<0.01	–0.38	<0.01	0.32	<0.01
concentration of dust particles	0.14	0.04	**–0.40**	<0.01	0.15	0.02
grain size	**–0.48**	**<0.01**	0.36	<0.01	**–0.43**	<0.01

5.2.4 Small fluctuations in COF and related conditions

One clear advantage of DTM is its ability to estimate fluctuations over a unit length of an ice core, represented as SD. The correlation between the SD and detrended $\Delta\varepsilon$ data indicates that more/less deformed ice exhibits smaller/larger fluctuations within the ice core sample, respectively. We compared the SD values and detrended $\Delta\varepsilon$, as well as concentrations of dust particles and Cl^- ions and grain sizes in Figure 11. We divided the time-series graph into two segments, before and after 350 kyr BP, each with differently scaled inverted SD values on the left axis. Here, 350 kyr BP corresponds to a depth of about 2520 m. In each panel, black, red, brown, purple, and light blue lines indicate SD (with left axis), detrended $\Delta\varepsilon$, concentration of dust particles, and Cl^- ions and grain sizes (with right axis), respectively. Note that the concentrations of dust particles and Cl^- ions, are and grain sizes represented on a logarithmic scale. We find that logarithmic concentration of dust and Cl^- ions and changes of grain sizes have variations very similar to inverted SD values. This similarity suggests that even a small amount of either dust particles or Cl^- ions (less than 30 ppbv for dust particles and 100 µg L^{-1} for Cl^- ions), or both, significantly influence ice deformation during interglacial periods.

We propose that these correlations are explained as follows. Dust concentration is essentially a control factor for grain boundary migration and thus for grain growth. The SD can be large when restriction for grain boundary migration is weak. In deep zones such as the LO20%, nucleated grains have a significant impact on the large SD. Grain size can be explained with the same context; grains can grow more when restriction for grain boundary migration is weak. The correlation between the SD and Cl⁻ ions remains unclear. On one hand, Cl⁻ ions dissolved in the ice crystal lattice appear to have no direct physical link with grain size, as determinant factor is likely dust. On the other hand, concentration of Cl⁻ ions is probably related to concentration of salt particles that can affect grain boundary migration. In any case, we do not find possible physical bases as to why the SD is correlated to logarithm of dust, grain size or concentration of ions. Additionally, it should be noted that the densification of firn is also correlated with logarithmic concentrations of impurities (e.g., Freitag et al., 2013, Fujita et al., 2016). Jones (1967) suggested that the deformation of ice is most likely related to the logarithm of the ionic concentrations. There may be a common underlying mechanism.

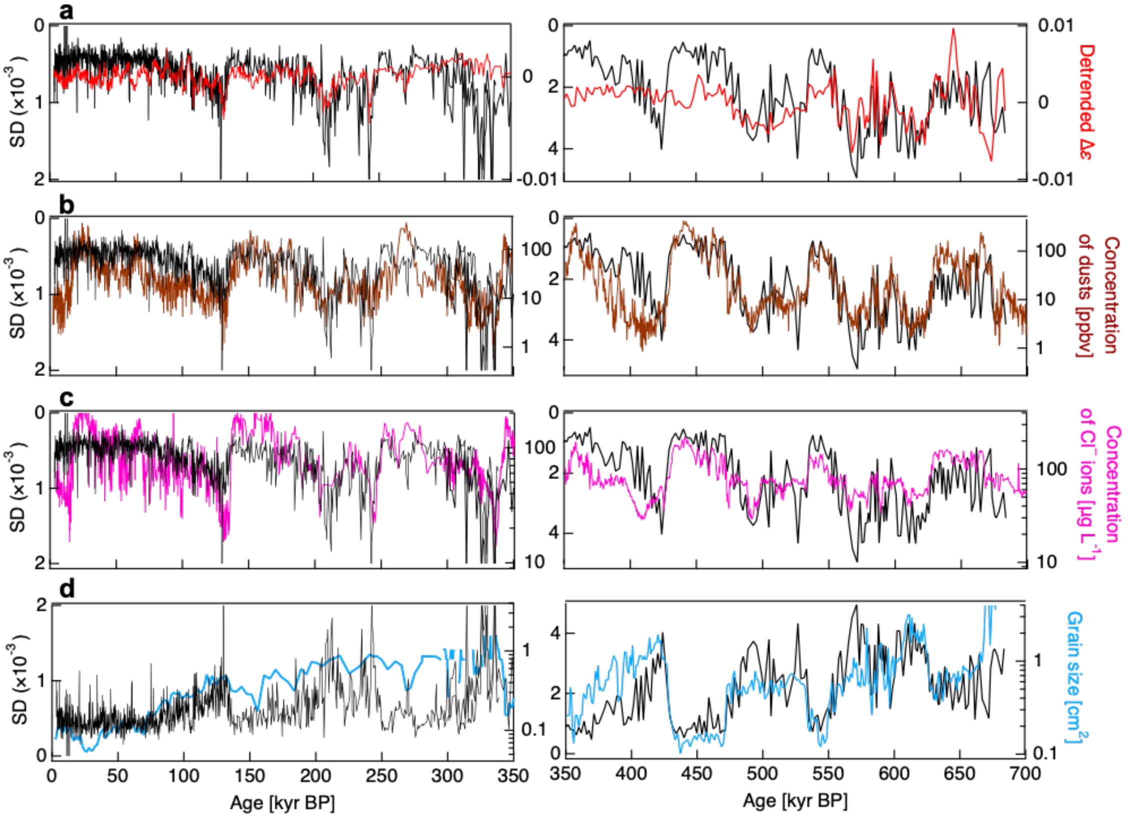

Figure 11. Comparison between SD values of Δε and physicochemical properties. (a) Comparison of SD values of Δε (black profiles using the left axis) with detrended Δε (red profiles using the right axis), (b) concentrations of dust particles (brown profiles using the right axis), (c) Cl⁻ ions (magenta profiles using the right axis) and (d) grain sizes (light blue profiles using the right axis) versus age. Panels display two

ranges of the SD scale based on age (0–350 and 350–700 kyr BP). The left axis in panels a–c is inverted to better highlight the close similarity in profile shapes. Concentrations of dust particles and Cl^- ions, and grain sizes are shown using logarithmic scales.

5.3 Microstructure at the deeper part of the DF ice core

5.3.1 Microscopic grain boundary sliding via microshear

Based on discussions above, in this section, we discuss the $\Delta\varepsilon$ value variations, focusing on microshear and dynamic recrystallization process. From microstructural observations, we identified interesting features in the impure layers (Figure 6): the crystal grains elongate, and their major axes incline away from horizontal directions. We introduce the term "microshear" to describe the localized stress/strain (Drury and Humphreys, 1988; Bons and Jessell, 1999; Faria et al., 2009). Detailed microstructures are shown in Figures 12a and 12b. The same feature, known as the "brick-wall pattern" has been observed at the high-impurity ice layers of the EDML ice core in Antarctica (see Figure 1a for location) (Faria, 2009; Weikusat et al., 2017) and the NEEM ice core in Greenland (Kuiper et al., 2020), but it has not been reported in the EDC ice core. The brick-wall pattern is formed by microscopic grain boundary sliding (GBS) via microshear (Faria et al. 2009; Llorens et al. 2016). A combination of high impurity content, temperature, and moderate stress causes GBS. These conditions are achieved in the bottom part of the ice sheets. Dislocation movement produces microshear zones along GB chains, splitting grains and creating sGBs. GBS accommodates deformation and reduces stress concentration. Consequently, dislocation creep is enhanced in these transient, localized zones of microshear. The formation of microshear bands creates new, flat GBs parallel to the shear plane, resulting in the brick-wall pattern.

Regarding the influence of GBS on the COF development, Faria et al. (2009) suggested that GBS has no severe impact on COF. In our study, we observed significant variations in $\Delta\varepsilon$ values within the impure layers. Furthermore, the $\Delta\varepsilon$ value has an inverse correlation with the dust concentration within the impure layer. Assuming COF remains unchanged by GBS, the variations in COF observed in the impure layers at greater depths would have originated at shallower depths before the onset of GBS. We observe an inverse correlation between the $\Delta\varepsilon$ value and dust concentration even at depths shallower than 2400 m. Another feature in the impure layer is approximately constant (or small fluctuation) grain size (Figure 9d). In the DF ice core, a constant grain size is observed between depths of 2640 and 2675 m, where the concentration of dust particles is extremely high. This constant grain size in ice core is known as "steady state grain size" (e.g., Steinbach et al., 2017). It is believed that steady state grain size is achieved when normal grain growth counteracts rotation recrystallization regardless of the initial grain size (Jacka and Li, 1994). We believe that the steady grain sizes in the impure layers established themselves after these layers had reached deeper depths. When the impure layers were at shallower depths in the past, grain size would have been inversely correlated with dust concentration. Besides rotational recrystallization, GBS also contributes to grain size reduction by dividing large grains into smaller ones through the formation of new grain boundaries.

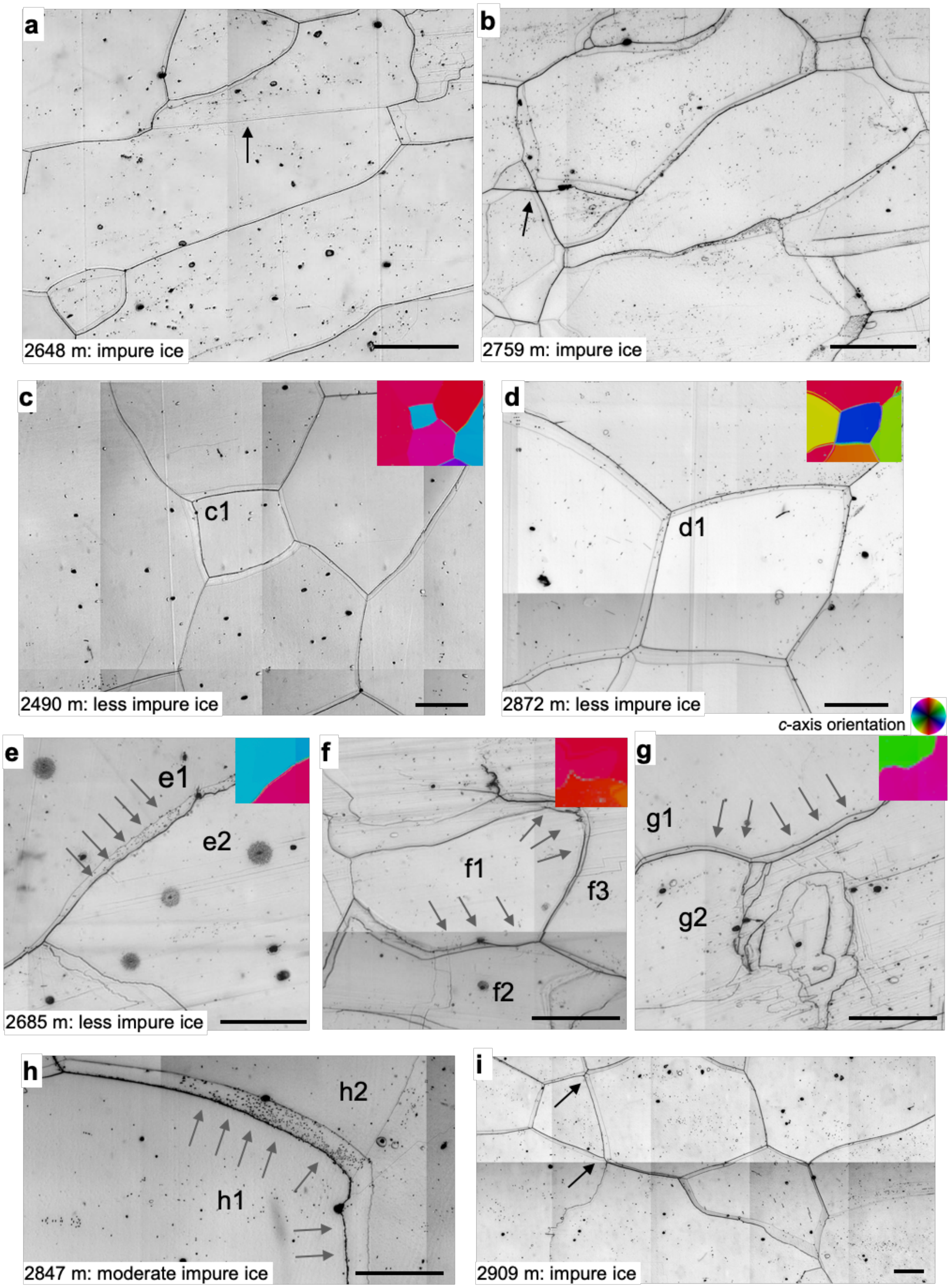
a
2648 m: impure ice
b
2759 m: impure ice
c
c1
2490 m: less impure ice
d
d1
2872 m: less impure ice
c-axis orientation
e
e1
e2
2685 m: less impure ice
f
f1
f2
f3
g
g1
g2
h
h1
h2
2847 m: moderate impure ice
i
2909 m: impure ice

https://doi.org/10.5194/egusphere-2023-3146
Preprint. Discussion started: 5 January 2024

Figure 12. Microstructure images for showing features of microshear and dynamic recrystallization. Images from seven selected depths are presented. Depths are indicated in each panel and summarized at the top of Figure 10. All images were observed using vertical thin sections. Black solid lines indicate GBs. GBs on the reverse side of a thin section are visible as thin lines. (a) and (b): Slanted brick-wall pattern was observed in the impure layer at 2648 and 2759 m depth, respectively. Black arrows in panels (a) and (b) indicate sGBs transitioning into GBs and quadruple junctions. (c) and (d): Examples of grains thought to have nucleated (2490 and 2872 m). Small and squat grains (c1 and d1) exhibit *c*-axis orientations different from surrounding grains and lack internal structures such as slip bands and sGBs. Panels (e) to (g) show examples from a depth of 2685 m. Gray arrows from (e) to (h) indicate migrating GBs. (e): Top-left large grain (e1) grows toward adjacent grain (e2). Migration direction can be read by observing absence and presence of the sGBs or slip bands; migrations erase such features. (f): Central grain (f1) grows toward grains f2 and f3. At the boundaries between grains e1-e2 and f1-f2, we observe pinning by impurities. Boundary migration is restricted by impurities. (g): Top large grain (g1) grows toward bottom grain (g2) having much and complicated sGBs. Color coding in panels (c) to (g) indicates the *c*-axis orientation of each grain. The legend for COF images is displayed at the center right. The red-colored grains have a *c*-axis oriented vertically, while green or blue-colored grains are inclined horizontally. (h): We observe segregation of dust particles on the front of migrating GB at 2847 m depth. (i): Microstructure at 2907 depth. Quadruple junctions are indicated by black arrows. Although the concentration of dust particles is high, there are no evident brick-wall patterns. Scale bars: 2mm.

5.3.2 Influence of nucleation and migration recrystallization on COF development

In dynamic recrystallization processes, rotation recrystallization has minimal effect on COF changes but reduces grain size. In contrast, migration recrystallization and grain nucleation (GN) can significantly modify COF (e.g., Cuffey and Paterson, 2010). In GN, new grains tend to form with a preferential orientation towards basal glide. As a result, new grains lead to a weakened concentration of the *c*-axis. When a difference in stored strain energy exists between two neighboring grains, the GB migrates towards the higher-energy grain. This recrystallization process is known as migration recrystallization. During migration recrystallization, GBs sometimes become irregular, forming interlocking patterns (Duval and Castelnau, 1995; Faria et al., 2014b). GN decreases the mean grain size; in contrast, migration recrystallization increases the mean grain size by consuming a neighbor grain.

Even when grain nucleation (GN) occurs in ice, its contribution to COF changes may not be immediately apparent in the volume-weighted average $\Delta\varepsilon$ values in the DTM. However, if such nucleated grains grow by incorporating water molecules from surrounding grains, the situation changes. Migration recrystallization significantly affects the $\Delta\varepsilon$ values if the grains having different *c*-axis orientations grow. Rotation recrystallization was observed at upper part of the DF and throughout of the EDC ice cores, but clear evidence of GN and migration recrystallization have not been reported in both ice cores (Azuma et al., 1999; 2000; Durand et al., 2009). In contrast, at the DF core, we found substantial instances of direct and circumstantial evidence.

Microstructures indicative of dynamic recrystallization are depicted in Figures 12(c–i). We found migration recrystallization; migrating GBs are indicated with arrows. In panels c and d, small and squared grains (c1 and d1) with no internal structures can be nucleated-grains. The orientations of the *c*-axis in nucleated grains differ significantly from those in surrounding grains. Faria et al. (2009) mentioned that GN occurs at triple junctions or at GBs as two-sided grains. We observe

https://doi.org/10.5194/egusphere-2023-3146
Preprint. Discussion started: 5 January 2024

grains satisfying these conditions at greater depths. In panel e, e1 grain migrates toward e2 grain. Migrating grain e1 lacks internal structures, while e2 grain has many sGBs. The presence of numerous sGBs implies high stored strain energy (Faria et al., 2014b). The lack of internal structures in grain e1 suggests a rearrangement of water molecules within its crystal lattice. Similarly, in panels f and g, we can observe migrating boundaries. In each panel, the migrating boundaries have irregular shapes, exhibiting interlocking features. The *c*-axes of migrating grains (e1 and g1) deviate from the *c*-axis clustering axis (i.e., vertical direction indicated in red). We propose that GN and migration recrystallization lead to significant changes in COF; a decreasing in $\Delta\varepsilon$ values and less clustered COF can be explained only by growth of grains with different *c*-axis orientations. Such a situation would be impossible if migration recrystallization occurs without accompanying GN.

Conversely, few interlocking GBs were observed in the impure layer. Grain coarsening by migration recrystallization does not appear to occur since impurities restrict the GB migration (e.g., Cuffey and Paterson, 2010). Therefore, the COF change (decreasing of $\Delta\varepsilon$ values) caused by migration recrystallization would occur only in the less impure layer. Thus, the dynamic recrystallization process would have greatly contributed to the characteristic behavior of COF development and relatively higher $\Delta\varepsilon$ values in the impure layer than surrounding at greater depths.

As a phenomenon associated with GB migration, we found dust particles segregation (Figure 12h). Considering the GB geometry around the microparticle pinning, h1 grain grows toward h2 grain. Microparticles are accumulated on the front of migrating GB. Boundary migration in the deeper parts leads to the redistribution of soluble impurities and dust particles. Figure 12i shows a microstructure at a depth of 2909 m. Given the high concentration of dust particles, it is likely that the area experienced GBS via microshear. Evident brick-wall patterns are lost at deepest 4% thickness from the bed, but quadruple junctions still exist (shown by arrows). Due to high temperature close to melting point, the pattern could be lost by dynamic recovery and recrystallization.

5.4 Zoning of COF development in the DF ice core

Based on the profiles of physical properties (Figures 8 and 9), we propose characterizing the COF development of the DF ice core into five distinct zones. This zoning proposal aims to facilitate discussions about physical processes. (i) Ice sheet surface to bubble close-off depth at approximately 100 m, categorized as the *firn zone*. (ii) Bubble close-off to 2400 m, categorized as the *dislocation creep zone.* (iii) 2400–2650 m, categorized as the *transition zone*. (iv) 2600–2950 m, categorized as the *dislocation-creep/recrystallization zone*. (v) 2950 m–bedrock, categorized as the *ice-bed interface zone*. In the following, we summarize physical processes within these zones.

i. Ice sheet surface–bubble close off depth: *firn zone*

COF in firn is dominated by complex processes of metamorphism and initial deformation up to the bubble close off point. Initial conditions of snow deposition, such as accumulation rate, wind forcing, temperature and temperature gradient, have a large influence on the initial properties of snow (e.g., Colbeck, 1989; Inoue et al., 2023). The initial conditions in microstructures regarding COF were described in our previous paper (see Section 4.3 in Saruya et al., 2022b). In the firn stage, limited studies suggest that COF sometimes clusters around the vertical or is horizontally inclined at inland plateau sites in East Antarctica (e.g., Fujita et al., 2009, Calonne et al., 2017). $\Delta\varepsilon$ values of the DF cores at ~100 m depths are about 0.008–0.009 (Fujita et al., 2009, 2016), These values represent about 30% of the perfectly clustered COF. This $\Delta\varepsilon$ value is the initial value for the subsequent zones.

ii. Bubble close-off depth–2400 m: *dislocation creep zone*

The $\Delta\varepsilon$ values increase with increasing depth from approximately 0.008 to 0.031 in this zone. The large-scale increasing trend is attributed to the rotation of the *c*-axes towards compressional axis due to dislocation creep.

iii. 2400–2650 m: *transitions zone*

This zone is characterized by a transition from the dominant deformation mechanism of dislocation creep to the onset of accompanying recrystallization processes. The $\Delta\varepsilon$ values reach maximum (approximately 0.031) and keep this high level in this zone. Additionally, fluctuations in $\Delta\varepsilon$ values are prevalent within this zone. Unlike the upper zones, the influence of bedrock topography starts to be apparent.

iv. 2650–2950 m: *dislocation-creep/recrystallization zone*

This zone is characterized by the predominance of recrystallization processes, which occur alongside the continued dislocation creep. As ice is deeper, the fluctuations of $\Delta\varepsilon$ values have a larger amplitude. In the impure layer, the $\Delta\varepsilon$ values remain at their highest levels; however, in surrounding less impure layers, the values are lower with numerous spikes of lower $\Delta\varepsilon$.

v. 2950 m–bedrock: *ice-bed interface zone*:

The deepest 3% zone of the ice sheet very close to the bedrock. The bottom ice is meteoric (Ohno et al., 2016). Crystal grains are often larger than diameter of the ice core (94mm). Thus, it is difficult to make statistically meaningful COF measurements. The temperature approaches the pressure melting point, at around –2 °C (Motoyama et al., 2020). We infer that prolonged exposure (in the range of 10^4–10^5 years) to this temperature has enhanced grain growth.

5.5 Implications for Ice Core Sciences and Radioglaciology

Based on the above discussions, we propose that polar ice sheets are massive bodies of ice, comprising alternating softer and harder layers, with layer thicknesses ranging from millimeters to those spanning glacial/interglacial periods. This situation has significant implications for ice core sciences and radioglaciology. First, these layered structures correlate directly with the vertical thinning of each layer, making them extremely useful for improving ice core dating models by providing constraints on strain values. Additionally, moving away from the dome, gravity-driven shear movement of the ice sheet leads to inhomogeneous deformation between layers or layer zones, resulting in the formation of folds, faults, and mixing of ice across various layer thickness scales. For ice core sciences aiming to investigate continuous records of very ancient ice (on the million-year scale), choosing a drilling site at the dome is crucial. Drilling away from the dome area may lead to serious problems due to layer disturbances. Another implication of this discussion concerns the state of radio echoes from the very deep parts, specifically, the lower 20% (LO20%) of the ice sheet. In glaciology, the presence or absence of echo-free zones is a topic of discussions (e.g., Fujita et al., 1999; Drews et al., 2009). In this study, we observed large fluctuations of $\Delta\varepsilon$ in a layered manner in the LO20% depth; $\Delta\varepsilon$ exhibited significant scatter in the less impure ice while the scatter was weak in the more impure ice. On one hand, the large scatter of $\Delta\varepsilon$ due to recrystallization will lead to rather incoherent scattering of radio waves in radar sounding. On the other hand, there are distinct large-scale layers of $\Delta\varepsilon$ on glacial/interglacial age scales. The amplitude of changes in permittivity between such large-scale layers is sufficiently large to cause detectable radio echoes. From this perspective, we can expect coherent permittivity-based radio echoes from deep within the ice sheets. However, at Dome Fuji, the layer was inclined by up to 45 degrees, a situation that prevents coherent scattering of radio waves. Moreover, moving away from the dome, continuous shear will disturb the preservation of layering, eventually forming radio echo-free zones. From the perspective of this ice core study, we suggest that the presence of echo-free zones in wide areas away from the dome can be reasonably explained.

6. Conclusions

For enhanced understanding of layer structures and deformation regimes in polar ice sheets, we investigated the DF ice core using innovative analytical methods. With the DTM, we provided COF data with unprecedented sampling frequency, spatial resolution, continuity, and statistical significance. Using the Laue X-ray diffraction method, we clarified detailed information about both *c*- and *a*-axes for each crystal grain. Furthermore, by combining data from these two methods, we clarified the COF layering in the LO20%. Coupled with previously reported COF data in the UP80%, we obtained comprehensive and high-resolution COF profiles for the core. Our major conclusions are summarized as follows:

Development of COF, Microstructure, and Layering

(i) The clustering strength of *c*-axes reached a maximum level at the bottom of the UP80% and in the transition zone (about 2400–2650 m depth), with large fluctuations below this zone.

(ii) COF fluctuates over distance scales ranging from 10^{-1} to 10^{2} m, depending on the concentration of ionic impurities, particularly Cl^{-} ions, and dust. Across the entire concentration range in logarithmic scale, these impurities significantly influence COF and deformation.

(iii) In the LO20%, the SD of the clustering strength within many 0.5-m ice segments is much larger than in the UP80%, indicating that COF fluctuation in short distances is enhanced in deeper parts.

(iv) In the LO20%, more impure layers maintain stronger clustering. In less impure layers, relaxation of the COF clustering occurs due to the emergence of new crystal grains with *c*-axis orientations distinct from the existing cluster, and dynamic recrystallization related to this emergence. Thus, dynamic recrystallization alters the COF of less impure layers.

(v) Signals of migration recrystallization, such as bulged and migrating GBs, were clearly found in less impure layers. The appearance of new crystal grains with *c*-axis orientation divergent from the cluster decreases the degree of *c*-axes clustering. Conversely, crystal grains in impure layers showed an elongated shape, with their major axes inclined from the horizontal. These microstructures are unique to deeper parts and result from GBS via microshear.

(vi) In impure layers, few signals of migration recrystallization were observed. The contrasting microstructures between impure and less impure layers are closely linked the differing variations in cluster strength in each layer.

(vii) The layer inclination angle shows stepwise changes at 2580 and 2770 m, being 10° at depths less than 2580 m, 20° at 2770 m, and reaching 45° at 3000 m. Similarly, the orientation of the *c*-axes cluster deviates from the vertical in deeper parts. Until a depth of 2700 m, the inclination angles of the *c*-axes cluster and layers are approximately consistent, but deviate from the vertical. The system rotates due to simple shear strain as a rigid body, while the *c*-axes cluster alone rotates backward, resulting from the compression components of the simple shear.

Common and Unique Features of Sites: Implications for Wider Areas in Polar Ice Sheets

(i) The fluctuations of the cluster strength versus ice age are common at DF and EDC, suggesting that depositional features such as chemistry and dust primarily determine these fluctuations. This suggests that COF layering is essentially common across a wide area of polar ice sheets, if the deposition of chemical ions and dust is similar among sites.

(ii) At the three summit sites in Antarctica (DF and EDC) and Greenland (GRIP), the depth zones where the maximum clustering appears are similar. The similarity among these three sites across both hemispheres may be more related to the total amount of strain, regardless of the temperature difference by about 10 °C in the LO20%.

(iii) In contrast to (i) above, features of layer inclinations in the DF ice core at greater depths were not observed in the EDC ice core, likely due to the DF drilling site's location above the subglacial slope at the bank of a drainage pathway for subglacial meltwater.

(iv) Unusual thickening of annual layers near the base of the DF ice core can be explained by the rigid body rotation of the system in the meridional direction near the bed of the ice sheet.

(v) COF development within the ice sheet was categorized into five zones.

(vi) We argue that the bottom 15% of the ice sheet plays a special role in shear deformation when the ice sheet moves away from the dome. Uneven strains between the layers will eventually compromise the integrity of the ice body in each part of the ice sheets. Consequently, folding, mixing, and faulting lead to the destruction of resolvable continuity in ice core signals, resulting in radio echo-free zones at this thickness. The rheology of ice should be assessed considering these folded and mixed states.

These findings warrant further examination for a better understanding. The new data and insights should link directly to key processes governing the flow of polar ice sheets. Expanding the knowledge from the dome summit to a three-dimensional dynamic layer structure within the ice sheet is a critical challenge. Deciphering radar sounding data in depth is key to this endeavor. The internal deformation of the ice sheet modulates flow based on COF, ion concentration, and microparticle presence, leading to differential ice movement or disturbances like folds and mixing at various layer thickness scales. These factors can introduce positive or negative feedback, modulating the flow characteristics of the ice sheet.

Data availability

The data used in this paper will be published in the National Institute of Polar Research ADS data repository in conjunction with the publication of the present manuscript in The Cryosphere.

Author contributions

We list author contributions using a standard called CrediT (Ghan et al., 2016) to achieve greater clarity in contributions of all authors. TS: Conceptualization, Methodology, Validation, Formal analysis, Investigation, Data curation, Writing - Original draft, Visualization. AM: Conceptualization, Methodology, Validation, Formal analysis, Investigation, Data curation, Writing - Review & editing, Visualization. SF: Conceptualization, Methodology, Validation, Formal analysis, Investigation, Writing - Original draft, Supervision, Project administration, Funding acquisition. TK: Investigation, Writing - Review & editing. MI: Investigation. KG-A, MH, AH, YI, HO, WS, and ST: Writing - Review & editing.

Competing interests

The authors declare that they have no conflict of interests.

Acknowledgements

The authors are grateful to all the Dome Fuji Deep Ice Core Project Members who contributed to obtaining the ice core samples, either through logistics, drilling, or core processing. The main logistics support was provided by the Japanese Antarctic Research Expedition (JARE), managed by the Ministry of Education, Culture, Sports, Science and Technology (MEXT). This work was supported by JSPS KAKENHI Grant Number 18H05294.

Appendix A: Abbreviations

COF: crystal orientation fabric

DF: Dome Fuji

DFICPM: Dome Fuji Ice Core Project Members

DTM: dielectric tensor method

EFZ: radio-echo free zone within polar ice sheets

GB: grain boundary

GN: grain nucleation

sGB: subgrain boundary

GBS: grain boundary sliding

HOCC: horizontal orientation of the *c*-axes cluster

IACC: inclination angle of the *c*-axes cluster from the vertical

IAVL: inclination angle of the visible layers

IPICS: International Partnerships in Ice Core Sciences

LO20%: the lowermost (deepest) ca. 20% thickness zone within Dome Fuji or more generally in polar ice sheets

MICC: median inclination of *c*-axes with reference to the axis of the *c*-axes cluster

UP80%: the uppermost (shallower) ca. 80% thickness zone within Dome Fuji or more generally in polar ice sheets

Appendix B: Consistency of the Δε' Values from the Two Resonators

In this study, we utilized an open resonator for microwaves operating at frequencies between 26.5 and 40 GHz (Resonator No.1), differing from our previous study that used frequencies of 15 and 20 GHz (Resonator No.2) (Saruya et al., 2022a, b), especially in terms of ice core sample size limitations. Using a high-frequency band allows for reduced sample dimensions due to the smaller beam diameter at higher frequencies. To verify the consistency between the current study (Resonator No.1) and the previous one (Resonator No.2), we conducted measurements of the Δε' across both frequency bands at depths of 2400 to 2500 m. Figure B1 presents a comparison of the dielectric anisotropy profiles and the standard deviation for each 0.5-m segment, using approximately 23 data points (0.02-m intervals) measured by both Resonator No.1 and Resonator No.2. No systematic differences were observed between the two resonators, though the standard deviation was slightly higher in Resonator No.1, due to its smaller beam diameter.

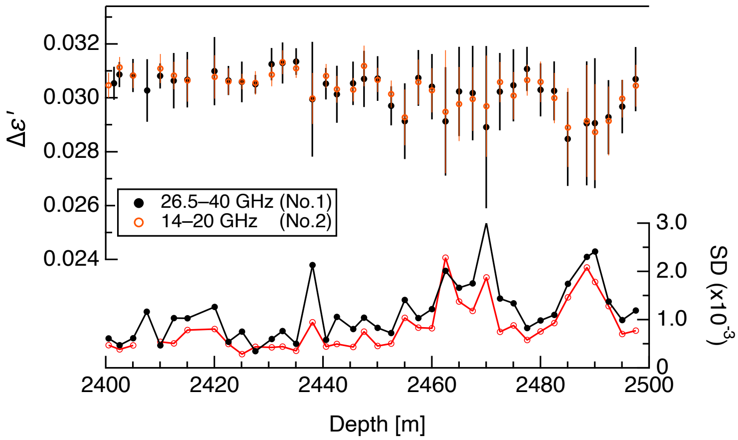

Figure B1. Comparison of the Δε′ and standard deviation measured by Resonator No.1 (black) and No.2 (red).

Appendix C: Inclination of the *c*-axes Cluster and the DTM

In the main text, Figure 2 was provided to explain the geometry of the sample and the open resonator. If the *c*-axes cluster aligns with the vertical (i.e., the ice core axis), it is relatively straightforward to set the angle between the *c*-axes cluster and the electric field close to about 45°. This was the case for ice shallower than approximately 2400 m (Saruya et al., 2022b). Figure C1a presents an example of this frame projected onto a Schmidt net. In this frame, the axis of the *c*-axes cluster is always orthogonal to the beam's incidence, thereby lying on the plane of the electric field vector. However, issues arise when the *c*-axes cluster deviates from the vertical. Depending on the inclination angle of the *c*-axes cluster from the zenith (IACC) and the rotation of the cylindrical ice core in horizontal directions, the axis of the *c*-axes cluster may not align with the plane of the electric field vector (refer to Figure C1b). In such cases, the DTM detects permittivity components projected onto the plane of the electric field vector. These are non-principal components of the tensorial permittivity. Consequently, the raw data of non-principal components of dielectric anisotropy, $\Delta\varepsilon'$ (as shown in Figure C1b), is smaller than the principal components of $\Delta\varepsilon$ when the axis of the *c*-axes cluster aligns with the plane of the electric field vector. Correction of data from $\Delta\varepsilon'$ to $\Delta\varepsilon$ is possible only if both the IACC and the horizontal orientation of the *c*-axes cluster (HOCC) are known (see Figure C1b’).

To enhance understanding of the measurement principles, Figure C1 is explained in greater detail here. Figure C1a depicts the case where the *c*-axes cluster of single pole fabric aligns with the vertical. The diagram's center represents the incident axis of the microwave beam in the resonator. Thus, the electric field vector is always orthogonal to the beam, spreading along the diagram's periphery. The dark blue plane contains the girdle of the *a*-axes. The red line represents a plane that includes both the beam axis and the *c*-axes cluster. In this setup, setting the electric field vector approximately within directions of $\boldsymbol{E}_1$ or $\boldsymbol{E}_2$ splits the vector components into two directions. This allows derivation of two permittivity components, ε_v and ε_h, as permittivities in the two principal axes along the diagram's periphery. Figure C1b illustrates a scenario where the *c*-axes cluster of single maximum fabric is inclined at an arbitrary horizontal orientation. The diagram's center is again the incident axis of the microwave beam. The dark blue plane contains the girdle of the *a*-axes, while the red line is a plane containing both the beam axis and the *c*-axes cluster. The dashed line represents a plane perpendicular to the red plane and containing the beam axis. In this arrangement, setting the electric field vector approximately within rotated directions of $\boldsymbol{E}_1$ or $\boldsymbol{E}_2$ still splits the vector components into two directions. However, it results in two non-principal components, ε'_v and ε'_h, as permittivity. Knowing the IACC (θ in Figure C1b’) and HOCC allows for accurate derivation of $\Delta\varepsilon$ values by horizontally rotating the frame to account for HOCC (as shown in Figure C1b’) and calculating the geometrical effects of the IACC.

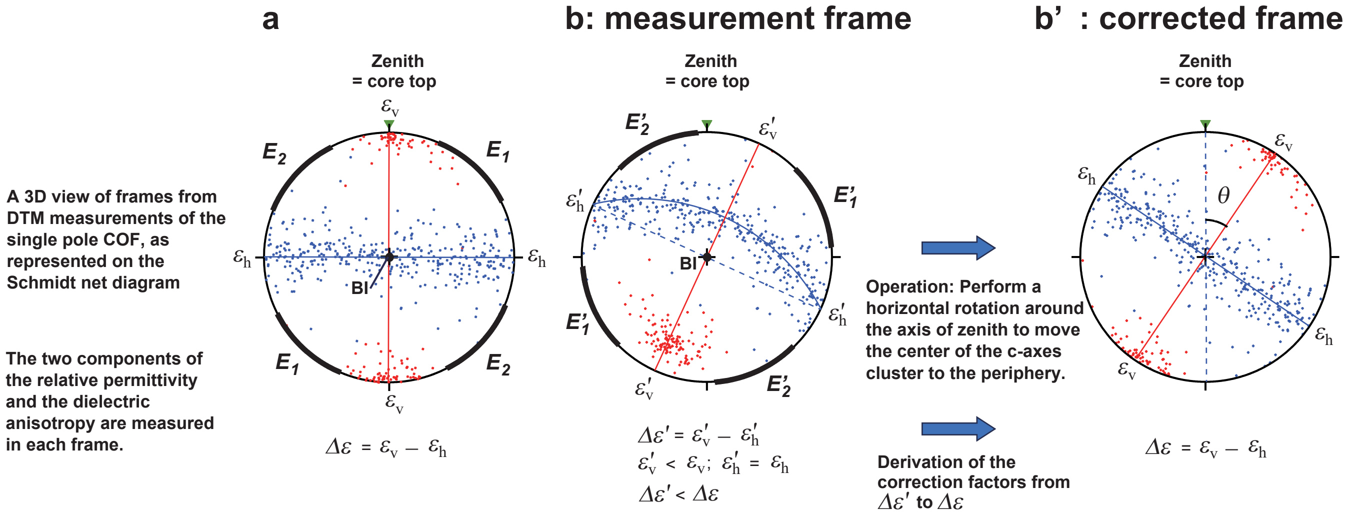

A 3D view of frames from DTM measurements of the single pole COF, as represented on the Schmidt net diagram

The two components of the relative permittivity and the dielectric anisotropy are measured in each frame.

Operation: Perform a horizontal rotation around the axis of zenith to move the center of the c-axes cluster to the periphery.

Derivation of the correction factors from $\Delta\varepsilon'$ to $\Delta\varepsilon$

Figure C1. An explanation of the 3D geometry of systems composed of core samples, crystal axes, and applied electric fields, represented using projections on the Schmidt net diagram. For three figures from (a) to (b’), both *c*-axes (red dots) and *a*-axes (dark blue dots) are presented for an imaginary ice core sample. In (a) and (b), the center of the diagram represents the axis of incidence for the microwave beam, with the peripheral circle forming a plane orthogonal to the beam. The top of this peripheral circle corresponds to the vertical orientation within the ice sheet, which is also the top of each ice core. Case (a): The *c*-axes cluster of single pole fabric aligns with the vertical, and the *a*-axes girdle lies on the horizontal plane. If the microwave beam's electric field vector falls within the orientation ranges of $\boldsymbol{E}_1$ or $\boldsymbol{E}_2$, it induces birefringence, allowing us to derive two components of permittivity, ε_v and ε_h, as principal components of the tensor. Consequently, we can calculate the difference as $\Delta\varepsilon$. Case (b): Here, the *c*-axes cluster of single pole fabric is inclined to an arbitrary horizontal orientation. The girdle of the *a*-axes deviates from the beam axis. In this scenario, using the electric field vectors from (a) within the orientation ranges of $\boldsymbol{E}_1$ or $\boldsymbol{E}_2$ is ineffective for detecting birefringence, as the splitting of waves into two components is not equally balanced. However, if the microwave beam's electric field vector is within inclined range from $\boldsymbol{E}_1$ or $\boldsymbol{E}_2$, namely $\boldsymbol{E}'_1$ or $\boldsymbol{E}'_2$, balanced birefringence is achieved, and we can derive two non-principal components of permittivity, ε'_v and ε'_h. This results in the calculation of the non-principal difference as $\Delta\varepsilon'$. Case (b’): This is the same as (b), but the system is horizontally rotated so that the *c*-axes cluster aligns with the periphery of the diagram where the electric field vector is located. By comparing permittivity values between cases (b) and (b’) using the COF data, we can determine factors to adjust $\Delta\varepsilon'$ values to $\Delta\varepsilon$ values.

Appendix D: Corrections from $\Delta\varepsilon$ to $\Delta\varepsilon'$

Using data from the Laue X-ray diffraction measurement taken at 43 different depths, we initially examined both the IACC and the HOCC. We assumed that the IACC consistently develops towards the same horizontal orientation within the ice sheet, a plausible assumption given the unlikelihood of horizontal rotation in ice flow under deep englacial conditions at the dome summit. The IACC is presented in Figure 5c of the main text. We observed that the HOCC gradually rotates with increasing depth (Figure D1). To address the data scatter, we proposed a fitting curve as shown in the figure. Notably, some data scatter between approximately 2400 and 2700 m leads to significant deviations from the fitting curve. We calculated the tensorial components of *c*-axes projected onto the diagram's periphery and further computed eigenvalue anisotropy (the difference between the maximum and minimum) by combining the IACC (Figure 5c) and the HOCC (Figure D1) for orientations where the *c*-axes cluster aligns with the periphery of the Schmidt net diagram (as shown in Figure C1b'). The results are presented in Figure D2. Using these data, we estimated coefficients for correcting $\Delta\varepsilon$ to $\Delta\varepsilon'$, detailed in Figure D3. We found that the necessary corrections are minor (up to several percent) at depths shallower than about 2730 m but become more significant at deeper depths (up to about 20 percent). At depths between approximately 2400 and 2730 m, where large deviations from the fitting curve were observed (Figure D1), the resulting errors in corrections are likely limited due to the IACC remaining small, less than about 20 degrees, in this depth range (Figure 5c). Therefore, we estimate the errors in our correction coefficients to be less than 10%.

Figure D4 displays the $\Delta\varepsilon'$ and $\Delta\varepsilon$ values, along with eigenvalue anisotropy obtained from the Laue X-ray diffraction measurements. At depths exceeding 2900 m, the corrections incorporate errors due to continuity uncertainties between core samples, which arise from unpredictable core rotation. Consequently, sudden changes in $\Delta\varepsilon$ values may be erroneous. Nevertheless, we observed a good agreement between the $\Delta\varepsilon$ values from the two ice cores (DF and EDC) at ages older than approximately 630 kyr BP, corresponding to the ice age at 2900 m.

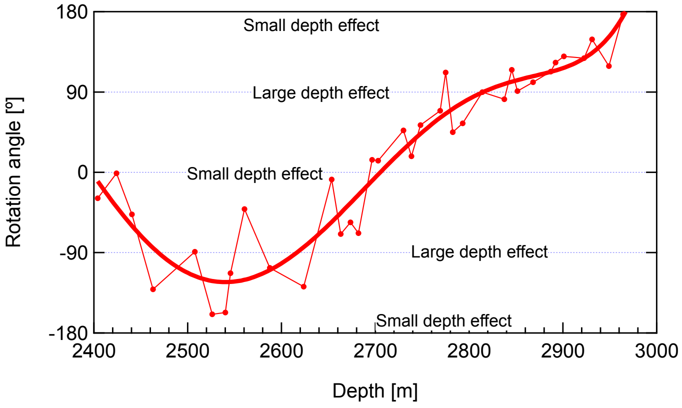

Figure D1. HOCC (left axis) was derived from the COF data obtained through the Laue X-ray diffraction measurements. Angles of 0, 180, or –180 degrees indicate that the *c*-axes cluster is perpendicular to the observer's line of sight and parallel to the electric field vector of the 845 electromagnetic waves. Conversely, angles of 90 or –90 degrees indicate that the *c*-axes cluster is parallel to the observer's line of sight and perpendicular to the electric field vector. When the HOCC measures 0, 180, or –180 degrees, it aligns with the periphery of the Schmidt equal area projection.

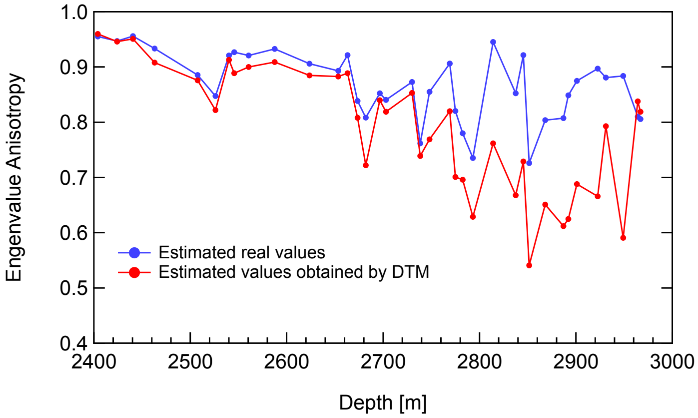

850 **Figure D2**. Comparison of eigenvalue anisotropy values between measurement frame (indicated in red) and corrected frame (indicated in blue).

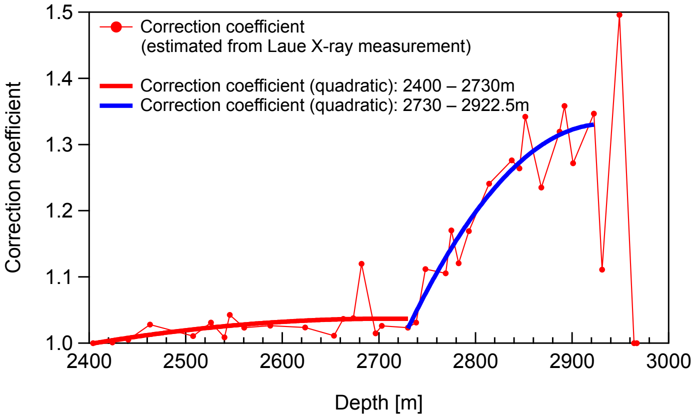

Figure D3. Correction coefficients for converting Δε' to Δε. This figure presents proposed fitting curves for depths ranging from 2400 to 855 2730 m and for depths greater than 2730 m.

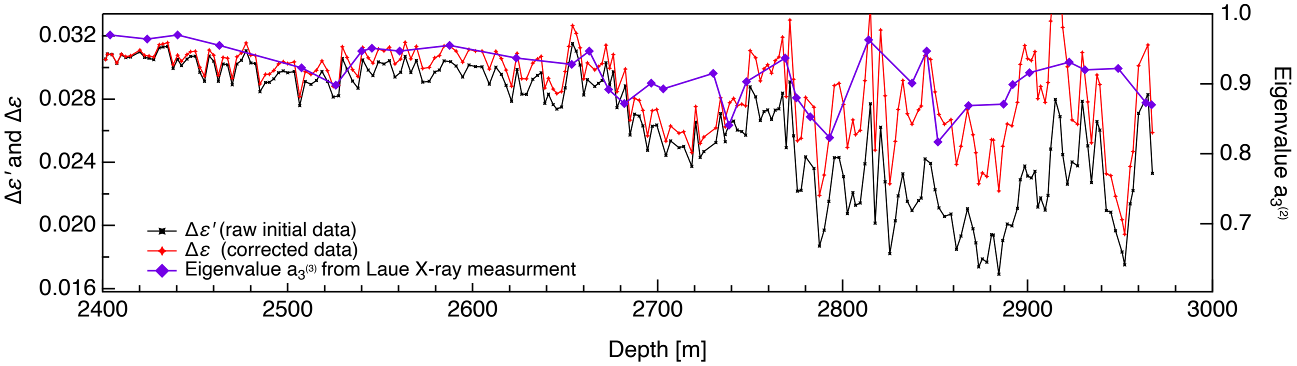

Figure D4. Correction of $\Delta\varepsilon'$ (depicted in black) to $\Delta\varepsilon$ (shown in red) and comparison with eigenvalues $a_3^{(2)}$ (illustrated in purple) as estimated from the Laue X-ray Diffraction Measurements. It is important to note that the DTM data represent average values for each 0.5 m section using thick-sections, while the Laue X-ray diffraction measurement data are derived from thin sections. The volume of ice represented by a single data point differs by approximately 10^2 times. Additionally, the DTM method provides volume-weighted values of COF, whereas the Laue X-ray diffraction measurements yield an average value across the total number of crystal grains, typically not accounting for the size (volume) of each individual crystal grain.

865 ## Appendix E: Continuous Variations in Δ*ε* and Comparison with Microstructures

Figure E1 showcases examples of the continuous variation of Δ*ε* across 0.5 m core samples at five depths (125.0–125.5, 1300.0–1300.5, 2648.0–2648.5, 2707.0–2707.5, and 2823.0–2823.5 m). The shallowest 2 depths were obtained from Saruya et al. (2022b). The mean values and standard deviations for each 0.02 m segment were calculated using various TEM $_{0,\,0,\,q}$ resonance modes in the open resonator method. For the data in Figure E1, the mean values (and SD) at these five depths are 870 0.0076 (0.0005), 0.0194 (0.0006), 0.0285 (0.0008), 0.0263 (0.0036), and 0.0282 (0.0043), respectively. Fluctuations within the 0.5 m ice core samples become more pronounced at greater depths. However, in the core sample with a higher concentration of dust particles (at 2648.0 m, represented by brown plots), the fluctuations are not as marked.

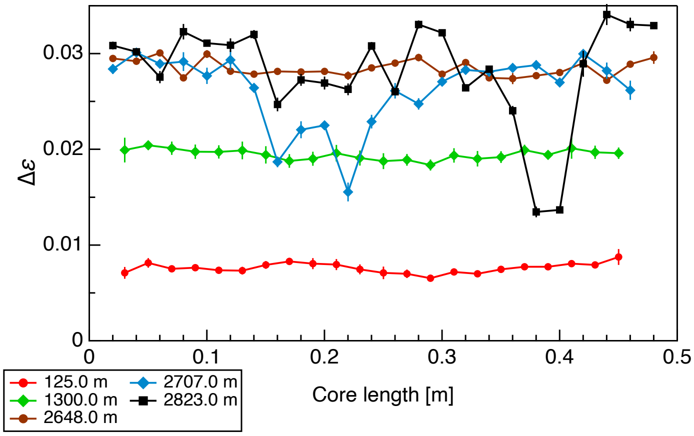

875 **Figure E1.** Examples of variations in Δ*ε* along 0.5 m sections of ice cores, as determined by continuous measurements. The bars display standard deviations derived from various resonance modes in the open resonator.

Figure E2 presents an example of comparing the Δ*ε* profile with microstructures, specifically for the 2490.0–2490.5 m sample. The upper and lower panels show fabric data and polarized images, respectively. Within the Δ*ε* profile, two locations 880 exhibit lower Δ*ε* values (at 0.11 and 0.27 m). At these depths, grains are observed with *c*-axis orientations differing from those of the surrounding grains. These layers contribute to a decrease in the mean Δ*ε*' value and an increase in the SD value for this 0.5 m core section.

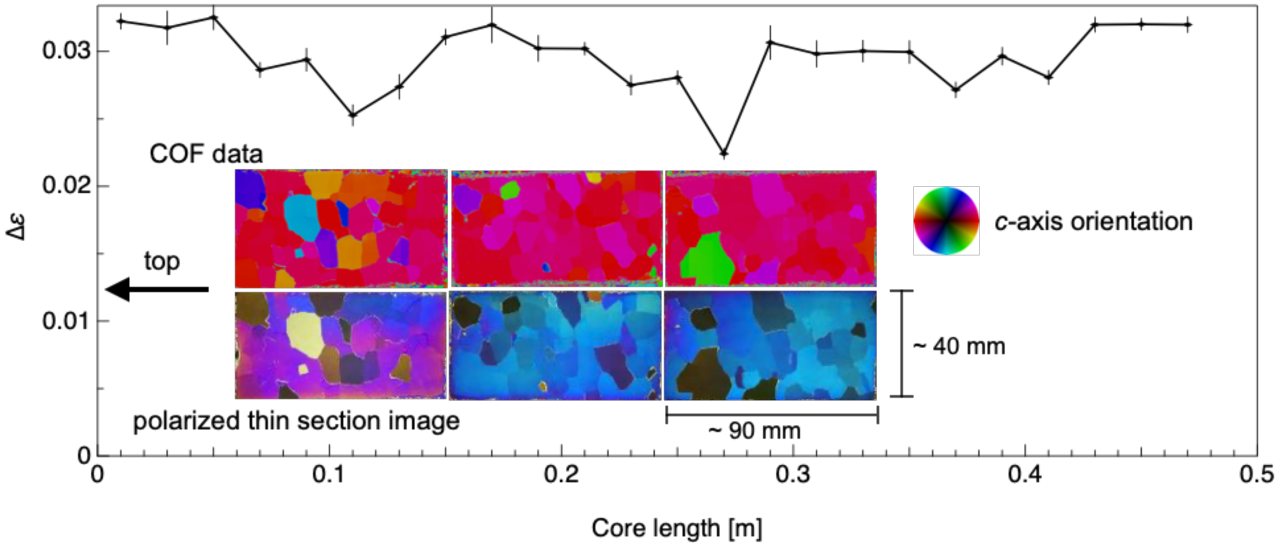

885 **Figure E2.** An example of comparing the $\Delta\varepsilon$ variation along a 0.5 m ice core section with microstructures (COF data and polarized images) obtained from thin-section measurements (2490.0–2490.5 m). The bars in the $\Delta\varepsilon$ variation graph represent standard deviations from different resonance modes of the open resonator. The horizontal scales in both the $\Delta\varepsilon$ variation graph and the microstructural images are aligned for consistency.

References

Alley, R. B., and Woods, G. A.: Impurity influence on normal grain growth in the GISP2 ice core, Greenland, J. Glaciol., 42(141), 255–260, https://doi.org/10.3189/S0022143000004111, 1996.

Azuma, N., Wang, Y., Mori, K., Narita, H., Hondoh, T., Shoji, H., and Watanabe O.: Textures and fabrics in the Dome F (Antarctica) ice core, Ann. Glaciol., 29, 163–168, https://doi.org/10.3189/172756499781821148, 1999.

Azuma, N., Wang, Y., Yoshida, Y., Narita, H., Hondoh, T., Shoji, H., and Watanabe, O.: Crystallographic analysis of the Dome Fuji ice core, in: Physics of Ice Core Records, edited by: Hondoh, T., Hokkaido University Press, Sapporo, 45–61, 2000.

Bamber, J. L., Gomez-Dans, J. L., and Griggs, J. A.: Antarctic 1 km Digital Elevation Model (DEM) from combined ERS-1 radar and ICESat Laser satellite altimetry, in: National Snow and Ice Data Center, Digital media, Boulder, Colorado, USA, 2009.

Barnes, P. R. F., Wolff, E. W., Mader, H. M., Udisti, R., Castellano, E., and Röthlisberger, R.: Evolution of chemical peak shapes in the Dome C, Antarctica, ice core, J. Geophys. Res., 108, 4126, https://doi.org/10.1029/2002JD002538, 2003.

Bazin, L., Landais, A., Lemieux-Dudon, B., Toyé Mahamadou Kele, H., Veres, D., Parrenin, F., Martinerie, P., Ritz, C., Capron, E., Lipenkov, V., Loutre, M.F., Raynaud, D., Vinther, B., Svensson, A., Rasmussen, S. O., Severi, M., Blunier, T., Leuenberger, M., Fischer, H., Masson-Delmotte, V., Chappellaz, J., and Wolff, E.: An optimized multi-proxy, multi-site Antarctic ice and gas orbital chronology (AICC2012): 120–800 ka, Clim. Past, 9(4), 1715–1731, https://doi.org/10.5194/cp-9-1715-2013, 2013.

Bons, P. D., and Jessell, M. W.: Micro-shear zones in experimentally deformed octachloropropane, J. Struct. Geol., 21(3), 323–334, https://doi.org/10.1016/S0191-8141(98)90116-X, 1999.

Buizert, C., Fudge, T. J., Roberts, W. H. G., Steig, E. J., Sherriff-Tadano, S., Ritz, C., Lefebvre, E., Edwards, J., Kawamura, K., Oyabu, I., Motoyama, H., Kahle, E. C., Jones, T. R., Abe-Ouchi, A., Obase, T., Martin, C., Corr, H., Severinghaus, J. P., Beaudette, R., Epifanio, J. A., Brook, E. J., Martin, K., Chappellaz, J., Aoki, S., Nakazawa, T., Sowers, T., Alley, R., Ahn, J., Sigl, M., Severi, M., Dunbar, N. W., Svensson, A., Fegyveresi, J., He, C., Liu, Z., Zhu, J., Otto-Bliesner, B., Lipenkov, V., Kageyama, M., and Schwander, J.: Antarctic-wide surface temperature and elevation during the Last Glacial Maximum, Science, 372, 1097–1101, https://doi.org/10.1126/science.abd2897, 2021.

Calonne, N., Montagnat, M., Matzl, M., and Schneebeli M.: The layered evolution of fabric and microstructure of snow at Point Barnola, Central East Antarctica, Earth Planet. Sci. Lett., 460, 293–301, https://doi.org/10.1016/j.epsl.2016.11.041, 2017

Church, J., Clark, P., Cazenave, A., Gregory, J, Jevrejeva, S., Levermann, A., Merrifield, M., Milne, G., Nerem, R., Nunn, P., Payne, A., Pfeffer, W., Stammer, D. and Unnikrishnan, A.: Sea Level Change. In: Climate Change 2013: The Physical Science Basis. Contribution of Working Group I to the Fifth Assessment Report of the Intergovernmental Panel on Climate Change (IPCC), Cambridge University Press, Cambridge, 1137–1216, 2013.

Colbeck, S. C.: Snow-crystal growth with varying surface temperatures and radiation penetration, J. Glaciol., 35(119), 23–29, https://doi.org/10.3189/002214389793701536, 1989.

Cuffey, K. M., and Paterson, W. S. B.: The Physics of Glaciers, 4th edition, Elsevier, Amsterdam, 2010.

Cullen, A. L.: Infrared and Millimeter Waves, in Millimeter-Wave Open-Resonator Techniques, Academic Press, New York, pp. 233–280, 1983.

Dahl-Jensen, D., Johnsen, S. J., Hammer, C. U., Clausen, H. B., and Jouzel, J.: Past Accumulation rates derived from observed annual layers in the GRIP ice core from Summit, Central Greenland, In: Peltier, W.R. (eds) Ice in the Climate System. NATO ASI Series, vol 12. Springer, Berlin, Heidelberg. https://doi.org/10.1007/978-3-642-85016-5_29, 1993.

Dahl-Jensen, D., Mosegaard, K., Gundestrup, N., Clow, G. D., Johnsen, S. J., Hansen, A. W., and Balling, N.: Past Temperatures Directly from the Greenland Ice Sheet, Science, 282, 268–271, https://doi.org/10.1126/science.282.5387.268, 1998.

De La Chapelle, S., Castelnau, O., Lipenkov, V., and Duval, P.: Dynamic recrystallization and texture development ice as revealed by the study of deep ice cores Antarctica and Greenland, J. Geophys. Res., 103, 5091–5105, https://doi.org/10.1029/97JB02621, 1998.

Dome Fuji Ice Core Project Members: State dependence of climatic instability over the past 720,000 years from Antarctic ice cores and climate modeling, Sci. Adv., 3(2), e1600446, https://doi.org/10.1126/sciadv.1600446, 2017.

Drews, R., Eisen, O., Weikusat, I., Kipfstuhl, S., Lambrecht, A., Steinhage, D., Wilhelms, F., and Miller, H.: Layer disturbances and the radio-echo free zone in ice sheets, The Cryosphere, 3, 195–203, https://doi.org/10.5194/tc-3-195-2009, 2009.

Drury, M., and Humphreys, F.: Microstructural shear criteria associated with grain-boundary sliding during ductile deformation, J. Struct. Geol., 10(1): 83–89, https://doi.org/10.1016/0191-8141(88)90130-7, 1988.

Durand, G., Weiss, J., Lipenkov, V., Barnola, J., Krinner, G., Parrenin, F., Delmonte, B., Ritz, C., Duval, P., and Röthlisberger, R.: Effect of impurities on grain growth in cold ice sheets, J. Geophys. Res., 111(F1)., F01015, https://doi.org/10.1029/2005JF000320, 2006.

Durand, G., Svensson, A., Persson, A., Gagliardini, O., Gillet-Chaulet, F., Sjolte, J., Montagnat M., Dahl-Jensen, D.: Evolution of the texture along the EPICA Dome C ice core, in: Physics of Ice Core Records II, edited by: Hondoh, T., Hokkaido University Press, Sapporo, 91–105, 2009.

Duval, P. and Castelnau, O.: Dynamic recrystallization of ice in polar ice sheets, J. Phys. III, 5, 197–205, https://doi.org/10.1051/jp4:1995317, 1995.

Eisen, O., Steinhage, D., Karlsson, N. B., Binder, T., Helm, V.: Ice thickness of Dome Fuji region, Antarctica, recorded with the AWI airborne radar system: line 20172048. PANGAEA, https://doi.org/10.1594/PANGAEA.920649, 2020.

EPICA Community Members: Eight glacial cycles from an Antarctic ice core, Nature, 429, 623–628, https://doi.org/10.1038/nature02599, 2004.

Faria, S. H., Kipfstuhl, S., Azuma, N., Freitag, J., Weikusat., I., Murshed, M. M., and Kuhs, W. F.: The Multiscale Structure of Antarctica Part I: Inland Ice, in: Physics of Ice Core Records II, edited by: Hondoh, T., Hokkaido University Press, Sapporo, 39–59, 2009.

Faria, S. H., Weikusat, I., and Azuma, N.: The microstructure of polar ice. Part I: Highlights from ice core research, J. Struct. Geol., 61, 2–20, http://dx.doi.org/10.1016/j.jsg.2013.09.010, 2014a.

Faria, S. H., Weikusat, I., and Azuma, N.: The microstructure of polar ice. Part II: State of the art, J. Struct. Geol., 61, 21–49, http://dx.doi.org/10.1016/j.jsg.2013.11.003, 2014b.

Freitag, J., Kipfstuhl, S., Laepple, T., and Wilhelms, F.: Impurity-controlled densification: a new model for stratified polar firn, J. Glaciol., 59, 1163–1169, https://doi.org/10.3189/2013JoG13J042, 2013.

Fujita, S., Maeno, H., Uratsuka, S., Furukawa, T., Mae, S., Fujii, Y., and Watanabe, O.: Nature of radio echo layer in the Antarctic ice sheet detected by a two-frequency experiment, J. Geophys. Res., 104(B6), 13013–13024, https://doi.org/10.1029/1999JB900034, 1999.

Fujita, S., Okuyama, J., Hori, A., and Hondoh, T.: Metamorphism of stratified firn at Dome Fuji, Antarctica: A mechanism for local insolation modulation of gas transport conditions during bubble close off, J. Geophys. Res., 114, F03023, https://doi.org/10.1029/2008JF001143, 2009.

Fujita, S., Holmlund, P., Matsuoka, K., Enomoto, H., Fukui, K., Nakazawa, F., Sugiyama, S., and Surdyk, S.: Radar diagnosis of the subglacial conditions in Dronning Maud Land, East Antarctica, The Cryosphere, 6, 1203–1219, https://doi.org/10.5194/tc-6-1203-2012, 2012.

Fujita, S., Goto-Azuma, K., Hirabayashi, M., Hori, A., Iizuka, Y., Motizuki, Y., Motoyama H., and Takahashi, K.: Densification of layered firn in the ice sheet at Dome Fuji, Antarctica, J. Glaciol., 62(231), 103–123, https://doi.org/10.1017/jog.2016.16, 2016.

Ghan, S., Crawford, J., Langematz, U., Leung, R., Li, Z., Russell, L., Steiner, A., and Zhang, C.: Author contributions can be clarified, J. Geophys. Res., 121, 8155–8155, https://doi.org/10.1002/2016JD025417, 2016.

Goodman, D. J., Frost, H. J., and Ashby, M. F.: The plasticity of polycrystalline ice, Philos. Mag., 43(3), 665–695, https://doi.org/10.1080/01418618108240401, 1981.

Goto-Azuma, K., Hirabayashi, M., Motoyama, H., Miyake, T., Kuramoto, T., Uemura, R., Igarashi, M., Iizuka, Y., Sakurai, T., and Horikawa, S.: Reduced marine phytoplankton sulphur emissions in the Southern Ocean during the past seven glacials, Nat. Commun., 10(1): 1–7, https://doi.org/10.1038/s41467-019-11128-6, 2019.

Hammonds, K. and Baker, I.: The effects of H_2SO_4 on the mechanical behavior and microstructural evolution of polycrystalline ice, J. Geophys. Res., 123, 535–556, https://doi.org/10.1002/2017JF004335, 2018.

Hargreaves, N. D.: The radio-frequency birefringence of polar ice, J. Glaciol, 21(85), 301–313, https://doi.org/10.3189/S0022143000033499, 1978.

Humphreys, F. and Hatherly, M.: Recrystallization and Related Annealing Phenomena, 2nd edn., Elsevier, https://doi.org/10.1016/B978-0-08-044164-1.X5000-2, 2004.

Inoue, R., Fujita, S., Kawamura, K., Oyabu, I., Nakazawa, F., and Motoyama, H.: Evolution of layered density and microstructure in near-surface firn around Dome Fuji, Antarctica, EGUsphere [preprint], https://doi.org/10.5194/egusphere-2023-1838, 2023.

Jacka, T. and Jun, L.: The steady-state crystal size of deforming ice, Ann. Glaciol., 20, 13–18, https://doi.org/10.3189/1994AoG20-1-13-18, 1994.

Jones, S. J.: Softening of ice crystals by dissolved fluoride ions, Phys. Lett. A, 25, 366–367, https://doi.org/10.1016/0375-9601(67)90702-5, 1967.

Jones, R. G.: The measurement of dielectric anisotropy using a microwave open resonator, J. Phys. D: Applied Physics, 9(5), 819–827, https://doi.org/10.1088/0022-3727/9/5/015, 1976a.

Jones, R. G.: Precise dielectric measurements at 35 GHz using an open microwave resonator, Proc. IEEE, 123(4), 285–290, http://doi.org/10.1049/piee.1976.0067, 1976b.

Jones, S., and Glen, J.: The effect of dissolved impurities on the mechanical properties of ice crystals, Philos. Mag., 19(157), 13–24, https://doi.org/10.1080/14786436908217758, 1969.

Komiyama, B., Kiyokawa, M., and Matsui, T.: Open resonator for precision dielectric measurements in the 100 GHz band. IEEE Trans. Microw. Theory Tech., 30(10), 1792–1796, https://doi.org/10.1109/22.88556, 1991.

Kuiper, E.-J. N., Weikusat, I., de Bresser, J. H. P., Jansen, D., Pennock, G. M., and Drury, M. R.: Using a composite flow law to model deformation in the NEEM deep ice core, Greenland – Part 1: The role of grain size and grain size distribution on deformation of the upper 2207 m, The Cryosphere, 14, 2429–2448, https://doi.org/10.5194/tc-14-2429-2020, 2020.

Langway, C. C.: Ice fabrics and the universal stage, SIPRE Tech. Rep., 62, 1958.

Lipenkov, V., Barkov, N., Duval, P., and Pimienta, P.: Crystalline Texture of the 2083 m Ice Core at Vostok Station, Antarctica, J. Glaciol., 35(121), 392–398, https://doi.org/10.3189/S0022143000009321, 1989.

Llorens, M.-G., Griera, A., Bons, P. D., Lebensohn, R. A., Evans, L. A., Jansen, D., and Weikusat, I.: Full-field predictions of ice dynamic recrystallisation under simple shear conditions, Earth Planet. Sci. Lett., 450, 233–242, http://dx.doi.org/10.1016/j.epsl.2016.06.045, 2016.

Miyamoto, A., Weikusat, I., and Hondoh, T.: Complete determination of ice crystal orientation using Laue X-ray diffraction method. J. Glaciol., 57(201), 103–110, https://doi.org/10.3189/002214311795306754, 2011.

Matsuoka, T., Mae, S., Fukazawa, H., Fujita, S., and Watanabe, O.: Microwave dielectric properties of the ice core from Dome Fuji, Antarctica, Geophys. Res. Lett., 25, 1573–1576, https://doi.org/10.1029/98GL01225, 1998.

Motoyama, H., Takahashi, A., Tanaka, Y., Shinbori, K., Miyahara, M., Yoshimoto, T., Fujii, Y., Furusaki, A., Azuma, N., and Ozawa, Y.: Deep ice core drilling to a depth of 3035.22 m at Dome Fuji, Antarctica in 2001–07, Ann. Glaciol., 62(85-86), 212–222, https://doi.org/10.1017/aog.2020.84, 2021.

Nakamura, T., and Jones, S.: Softening effect of dissolved hydrogen chloride in ice crystals, Scripta Metallurgica, 4(2), 123–126, https://doi.org/10.1016/0036-9748(70)90176-6, 1970.

Ohno, H., Igarashi, M., and Hondoh, T.: Salt inclusions in polar ice core: Location and chemical form of water-soluble impurities, Earth Planet. Sc. Lett., 232, 171–178, https://doi.org/10.1016/j.epsl.2005.01.001, 2005.

Ohno, H., Iizuka, Y., Hori, A., Miyamoto, A., Hirabayashi, M., Miyake, T., Kuramoto, T., Fujita, S., Segawa, T., Uemura, R., Sakurai, T., Suzuki, T., and Motoyama, H.: Physicochemical properties of bottom ice from Dome Fuji, inland East Antarctica, J. Geophys. Res., 121(7), 1230–1250, https://doi.org/10.1002/2015JF003777, 2016.

Oyabu, I., Kawamura, K., Buizert, C., Parrenin, F., Orsi, A., Kitamura, K., Aoki, S., and Nakazawa, T.: The Dome Fuji ice core DF2021 chronology (0–207 kyr BP), Quaternary Sci. Rev., 294, 107754, https://doi.org/10.1016/j.quascirev.2022.107754, 2022.

Oyabu, I., Kawamura, K., Fujita, S., Inoue, R., Motoyama, H., Fukui, K., Hirabayashi, M., Hoshina, Y., Kurita, N., Nakazawa, F., Ohno, H., Sugiura, K., Suzuki, T., Tsutaki, S., Abe-Ouchi, A., Niwano, M., Parrenin, F., Saito, F., and Yoshimori, M.: Temporal variations of surface mass balance over the last 5000 years around Dome Fuji, Dronning Maud Land, East Antarctica, Clim. Past, 19, 293–321, https://doi.org/10.5194/cp-19-293-2023, 2023.

Petrenko, V. F., and Whitworth, R. W.: Physics of Ice, Oxford University Press, Oxford, 1999.

Pattyn, F., Perichon, L., Aschwanden, A., Breuer, B., de Smedt, B., Gagliardini, O., Gudmundsson, G. H., Hindmarsh, R. C. A., Hubbard, A., Johnson, J. V., Kleiner, T., Konovalov, Y., Martin, C., Payne, A. J., Pollard, D., Price, S., Rückamp, M., Saito, F., Souček, O., Sugiyama, S., and Zwinger, T.: Benchmark experiments for higher-order and full-Stokes ice sheet models (ISMIP–HOM), The Cryosphere, 2, 95–108, https://doi.org/10.5194/tc-2-95-2008, 2008.

Pattyn, F.: Antarctic subglacial conditions inferred from a hybrid ice sheet/ice stream model, Earth Planet. Sc. Lett., 295(3–4), 451–461, https://doi.org/10.1016/j.epsl.2010.04.025, 2010.

Saruya, T., Fujita, S., and Inoue, R.: Dielectric anisotropy as indicator of crystal orientation fabric in Dome Fuji ice core: method and initial results, J. Glaciol., 68(267), 65–76, https://doi.org/10.1017/jog.2021.73, 2022a.

Saruya, T., Fujita, S., Iizuka, Y., Miyamoto, A., Ohno, H., Hori, A., Shigeyama, W., Hirabayashi, M., and Goto-Azuma, K.: Development of crystal orientation fabric in the Dome Fuji ice core in East Antarctica: implications for the deformation regime in ice sheets, The Cryosphere 16(7), 2985–3003, https://doi.org/10.5194/tc-16-2985-2022, 2022b.

Shoji, H., and Higashi, A.: A deformation mechanism map of ice, J. Glaciol., 85(21), 419–427, https://doi.org/10.3189/S002214300003358X, 1978.

Steinbach, F., Kuiper, E.-J. N., Eichler, J., Bons, P. D., Drury, M. R., Griera, A., Pennock, G. M., and Weikusat, I.: The Relevance of Grain Dissection for Grain Size Reduction in Polar Ice: Insights from Numerical Models and Ice Core Microstructure Analysis, Front. Earth Sci., 5, https://doi.org/10.3389/feart.2017.00066, 2017.

Thibert, E., and Domine F.: Thermodynamics and kinetics of the solid solution of HCl in ice, J. Phys. Chem. B, 101(18), 3554–ß3565, https://doi.org/10.1021/jp962115o, 1997.

Thorsteinsson, T., Kipfstuhl, J. and Miller, H.: Textures and fabrics in the GRIP ice core, J. Geophys. Res., 102(C12), 26583–26599, https://doi.org/10.1029/97JC00161, 1997.

Tsutaki, S., Fujita, S., Kawamura, K., Abe-Ouchi, A., Fukui, K., Motoyama, H., Hoshina, Y., Nakazawa, F., Obase, T., Ohno, H., Oyabu, I., Saito, F., Sugiura, K., and Suzuki, T.: High-resolution subglacial topography around Dome Fuji, Antarctica, based on ground-based radar surveys conducted over 30 years, The Cryosphere, 16, 2967–2983, https://doi.org/10.5194/tc-16-2967-2022, 2022.

Weikusat, I., Jansen, D., Binder, T., Eichler, J., Faria, S. H., Wilhelms, F., Kipfstuhl, S., Sheldon, S., Miller, H., Dahl-Jensen, D., and Kleiner, T.: Physical analysis of an Antarctic ice core – towards an integration of micro- and macrodynamics of polar ice, Phil. Trans. R. Soc. A, 375, 20150347, http://dx.doi.org/10.1098/rsta.2015.0347, 2017.

Wolff, E. W., Fischer, H., van Ommen, T., and Hodell, D. A.: Stratigraphic templates for ice core records of the past 1.5 Myr, Clim. Past, 18, 1563–1577, https://doi.org/10.5194/cp-18-1563-2022, 2022.

Yamanouchi, T., Hirasawa, N., Hayashi, M., Takahashi, S., and Kaneto, S.: Meteorological characteristics of Antarctic inland station, Dome Fuji. Mem. Natl Inst. Polar Res., Spec. Issue, 57, 94–104, 2003.

Young, D. A., Roberts, J. L., Ritz, C., Frezzotti, M., Quartini, E., Cavitte, M. G. P., Tozer, C. R., Steinhage, D., Urbini, S., Corr, H. F. J., van Ommen, T., and Blankenship, D. D.: High-resolution boundary conditions of an old ice target near Dome C, Antarctica, The Cryosphere, 11, 1897–1911, https://doi.org/10.5194/tc-11-1897-2017, 2017.